Impact of HF radar currents gap-filling methodologies on the Lagrangian assessment of coastal dynamics

Ismael Hernández-Carrasco[1], Lohitzune Solabarrieta[2], Anna Rubio[3], Ganix Esnaola[4], Emma Reyes[1], and Alejandro Orfila[5]

[1]ICTS-SOCIB, 07122, Palma, Spain
[2]King Abdullah University of Science and Technology (KAUST), Red Sea Research Center (RSRC), Biological and Environmental Sciences and Engineering Division (BESE), Thuwal 23955-6900, Saudi Arabia
[3]AZTI, Marine Ecosystems Functioning, 20110, Spain,
[4]UPV-EHU, 48080, Spain
[5]IMEDEA (CSIC-UIB), 07190, Esporles, Spain

Correspondence: Ismael Hernández-Carrasco (ihernandez@socib.es)

Abstract.

High-frequency radar, HFR, is a cost-effective monitoring technique that allows to obtain high-resolution continuous surface currents, providing new insights for understanding small-scale transport processes in the coastal ocean. In the last years, the use of Lagrangian metrics to study mixing and transport properties is growing in importance. A common condition among all the Lagrangian techniques is that complete spatial and temporal velocity data is required to compute trajectories of virtual particles in the flow. However, hardware or software failures in HFR system can compromise the availability of data, resulting in incomplete spatial coverage fields or periods without data. In this regard, several methods have been widely used to fill spatio-temporal gaps in HFR measurements. Despite the growing relevance of these systems there are still many open questions concerning the reliability of the gap-filling methods for the Lagrangian assessment of the coastal ocean dynamics. In this paper, we first develop a new methodology to reconstruct HFR velocity fields based on Self-Organizing Maps (SOM). Then a comparative analysis of this method with other available gap-filling techniques is performed, i.e. Open-Boundary Modal Analysis (OMA) and Data Interpolating Empirical Orthogonal Functions (DINEOF). The performance of each approach is quantified in the Lagrangian frame through the computation of finite size Lyapunov exponents, Lagrangian Coherent Structures and residence times. We determine the limit of applicability of each method regarding four experiments based on the typical temporal and spatial gaps distribution observed in HFR systems unveiled by a K-means clustering analysis. Our results show that even when a large number of data is missing, the Lagrangian diagnoses still give an accurate description of the oceanic transport properties.

1 Introduction

Knowledge of the spatial and temporal complexity of coastal processes is one of the major challenges in oceanography. Understanding the coastal hydrodynamics is crucial for quantifying the contribution of the coastal margins to the world ocean's biological productivity (Pauly et al., 2008; Cloern et al., 2014) and to the global CO_2 storage (Bauer et al., 2013). Large-scale

currents are strongly affected by the intricate orography and by the influence of the local boundary layers in coastal regions: the input of energy at the surface through heterogeneous heat fluxes and local wind forcing and the dissipation at the coast and at the seabed. This results in a complex coastal circulation characterized by the interaction of multiscale processes that requires specific numerical and observational approaches to properly study its variability (Haidvogel et al., 2000). High Fre-

5 quency Radars (HFRs) data can potentially be used to observe and provide information on these processes through hourly measurements of high resolution surface currents.

HFR systems were originally developed in Stewart and Joy (1974) and Barrick et al. (1977) to remotely sensing the state of the sea surface based on the back-scatter of HF radio waves. Over the last 20-25 years there has been a rapid growth in the use of coastal radars demonstrating the possibility of observing and monitoring the complex surface current dynamics, leading

10 to a fast spread of installations of HFR observatories in many coastal regions. Currently, HFR is the unique technology able to provide autonomously continuous hourly surface velocity measurements over wide coastal areas (typical range of 30-100 km from the coast) at high spatial (a few km) resolution depending on the working frequency (Paduan and Washburn, 2013; Bellomo et al., 2015; Lana et al., 2016; Rubio et al., 2017). Contrary to satellite altimetry, the use of HFR data can potentially provide gridded velocities with the necessary resolution in both space and time to unravel the role of small scales on the

15 dynamical properties (Hernández-Carrasco et al., 2018).

In particular, HFR observations are crucial for those applications associated with transport processes, not only addressing the study of marine ecosystems but also for a wide range of coastal activities. These include search and rescue operations (Ullman et al., 2006); predicting and mitigating the spread of oil spill or other pollutants (Lekien et al., 2005; Shadden et al., 2009); understanding the impact of transport and mixing properties on relevant biogeochemical properties such as the primary

20 productivity of plankton (Cianelli et al., 2017; Hernández-Carrasco et al., 2018); coastal larval transport or fishery management (Bjorkstedt and Roughgarden, 1997).

The Lagrangian approach addresses the effects of the velocity field on transported substances, which is of utmost relevance for studying transport processes. This approach has the advantage of exploiting both spatial and temporal variability of a given velocity field. They can even unveil sub-grid filaments generated by chaotic stirring, providing a more complete description

25 of transport phenomena. Specially, the concept of Lagrangian Coherent Structure (LCS, see the review by Haller, 2015) has been receiving growing attention in the last decades in geophysical sciences since it gives an unprecedented description of transport processes, identifying local maximizing lines of material stretching. These structures act as transport barriers and separate regions with different dynamical behavior, which are of great relevance for the marine biological dynamics (Tew Kai et al., 2009; Hernández-Carrasco et al., 2014; Bettencourt et al., 2015). The combination of Lagrangian techniques, including

30 LCS, residence times and Lagrangian divergence, allows to obtain an improved description of the flow geometry, providing new insights for understanding bio-physical interactions in coastal seas (Rubio et al., 2018; Hernández-Carrasco et al., 2018), as well as to localize convergence zones which are relevant for tracking oil-spill accumulation (Lekien et al., 2005) or jellyfish aggregations.

Lagrangian diagnoses require complete spatial and temporal velocity data to compute trajectories of synthetic particles.

35 However, HFR can fail due to external circumstances, i.e., environmental factors, or hardware or software malfunction, power

failure and communication disruptions at the radar stations, leading to incomplete measurements in the form of data gaps both in space and time. In general, the occurrence of gaps in the data follows a pattern that can be associated with a particular cause, for instance the instrumentation malfunction, sea state, signal interference, antenna configuration, facilitating their interpretation and simulation.

5   In this regard, different methodologies have been developed in the last years with the aim of filling velocity fields derived from HFR measurements. The most widely extended technique is the Open-Boundary Modal Analysis (OMA) (Kaplan and Lekien, 2007). Other methods have also been proved to be efficient, among others, the DINEOF method based on empirical orthogonal functions (Alvera-Azcárate et al., 2005), the functional method penalizing the OMA modes variability described in Yaremchuk and Sentchev (2009), and the DCT-PLS method based on penalized least squares regression method using a 10 three-dimensional discrete cosine transform (Fredj et al., 2016). Although the performance of some of these methods has been analyzed from the Eulerian point of view, that is, comparing the original and the reconstructed velocity fields (Kaplan and Lekien, 2007; Yaremchuk and Sentchev, 2009; Fredj et al., 2016), an assessment of the reliability of the Lagrangian metrics when computed using reconstructed data is still lacking.

    Here we introduce a new method based on unsupervised neural networks, the Self-Organizing Maps (SOM). Then, we 15 perform an intercomparison of this new methodology with OMA and DINEOF. We analyze the effect of these gap-filling methods on the Lagrangian computations derived from reconstructed HFR velocities in the SE region of the Bay of Biscay (BoB). Their robustness under different scenarios of data gaps are discussed.

    The paper is organized as follows. After this introduction, we first describe the data. Gap-filling methods used in the comparison, including the new method developed here are described in section 3. Section 4 is devoted to describe the different 20 data gap scenarios commonly found in the HFR system operating in the SE BoB and used in the evaluation. The results of the Eulerian and Lagrangian comparison are shown in section 5.

2   HF radar data

Two long-range CODAR Ocean Sensor SeaSonde HFR sites are operational in the SE BoB since 2009. Both antennas emit at a 40-kHz bandwidth centered at 4.5 MHz frequency and they are part of the Basque in situ operational oceanography 25 observational network owned by the Directorate of Emergency Attention and Meteorology of the Basque government's Security Department. The sites are located in Cape Higer and Cape Matxitako (Figure 1). The averaged Doppler backscatter spectrum obtained from the received signal (in a window of 3 h) is processed to obtain hourly radial currents using the MUSIC algorithm (Schmidt, 1986). The coverage of radial data is up to 150 km with a 5 km range cell resolution and 5º angular resolution. Radial data are quality controlled using advanced procedures based on velocity and variance thresholds, noise to signal ratios and radial 30 total coverage. Successful validation analysis for this HFR with surface drifters and mooring data have been previously done in Solabarrieta et al. (2014) and Rubio et al. (2011). Hourly HFR data for April 2012, April 2013 and April 2014 are used in this study due to the good spatial and temporal data coverage, as well as to avoid persistence in the dynamical conditions (e.g.

Solabarrieta et al., 2015). The whole 2014 data set has been used to characterize the most typical data-gap types observed in the HFR system of the SE BoB (see Sec. 4).
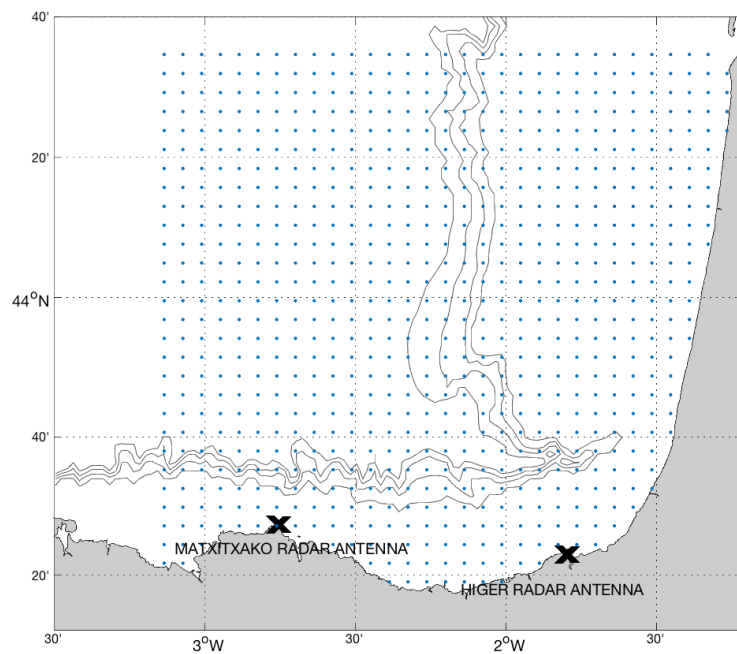
Figure 1. Map showing the location of the two antennas (Matxitxako and Higer) of the BoB HFR systems. The grid points of the total HFR velocity field are plotted in blue.

3 Gap-filling methods

3.1 OMA and DINEOF

Some methods, i.e the Open-boundary Modal Analysis (OMA) and the Data Interpolating Empirical Orthogonal Functions (DINEOF), are nowadays widely used to fill spatio-temporal gaps in HFR measurements. We briefly explain these two methods below.

The Open Modal Analysis (OMA, Kaplan and Lekien, 2007) is based on a set of linearly independent modes that are calculated before they are fit to the data. These modes describe all possible current patterns inside a two-dimensional domain (taking into account the open boundaries and the coastline). The amplitude of those modes is then fitted to current measurements inside the domain. The OMA analysis considers the kinematic constraints imposed on the velocity field by the coast since the OMA modes are calculated taking into account the coastline by setting a zero normal flow. Depending on these constraints they can be limited in representing localized small-scale features as well as flow structures near open boundaries. Besides, difficulties may arise when dealing with gappy data, especially when the horizontal gap size is larger than the minimal resolved length scale (Kaplan and Lekien, 2007) or when only data from one antenna is available. In the case of large gaps, unphysically fitted currents can be obtained if the size of the gap is larger than the smallest spatial scale of the modes, since the mode amplitudes are not sufficiently constrained by the data (Kaplan and Lekien, 2007). This is why when using OMA it is recommended to reach a compromise between the number of modes used for spatial scales larger than the largest gap and a sufficient number of modes correctly representing the spatial variance of the original fields (knowing that the spatial smoothing increases as the number of modes decreases). For this work, we used the OMA modules in the HFR Progs Matlab package (https://cencalarchive.org/ocmpmb/COCMPwiki/) to process radial velocities into total currents. Setting a minimum spatial scale of 20 km, 85 OMA modes were built for the regular grid shown in Figure 1. OMA is especially useful to obtain a solution in the base line area (i.e. the area between the two radar antennas where total currents cannot be computed directly from radial information) and has been used to provide fields to compute accurate trajectories (Solabarrieta et al., 2016; Hernández-Carrasco et al., 2018) and surface Lagrangian transport in coastal basins (Rubio et al., 2018; Hernández-Carrasco et al., 2018).

The Data Interpolating EOFs (DINEOF) is an EOF-based iterative methodology used to interpolate gaps or missing data in geophysical datasets (Beckers and Rixen, 2003; Alvera-Azcárate et al., 2005). The technique is applied to a $N \times M$ data matrix, where N is the size of spatial locations of the geophysical field, and M the time dimension of the data. Before the methodology is initialized, part of the initially non-missing data is removed from the data matrix, and stored for cross-validation. Then anomalies are computed by removing the time mean at each location, and gaps or missing data are replaced by zero value anomalies. At this point the data matrix is iteratively decomposed and rebuilt by means of an EOF analysis with a fixed number of EOFs. Values of originally missing gaps evolve through this iteration until convergence is met. Changing the number of EOFs, a set of such iterations is produced using a different number of EOFs in each repetition. The optimal number of EOFs is then deduced by cross-validation comparing the initially stored data with the different versions of the reconstructed data. Once the optimal number is deduced, the originally retained data are introduced back in the data matrix, and a final reconstruction is made using the optimal number of EOFs.

DINEOF was introduced by Beckers and Rixen (2003), Alvera-Azcárate et al. (2005) and Alvera-Azcárate et al. (2007) in both univariate and multivariate forms. The method was initially applied to Sea Surface Temperature and Ocean Color (e.g. Alvera-Azcárate et al., 2005; Ganzedo et al., 2011; Volpe et al., 2012; Esnaola et al., 2012; Beckers et al., 2014; Alvera-Azcárate et al., 2015), but the technique has also been used to other variables like Sea Surface Salinity (Alvera-Azcárate et al., 2016). The DINEOF Fortran code (http://modb.oce.ulg.ac.be/mediawiki/index.php/DINEOF) was applied to the combination of radial currents from the two antennas. The Matlab/Octave complementary sources provided with the Fortran codes are also used to produce cross-validation masks internally required by DINEOF, following the procedure proposed in Alvera-Azcárate et al. (2005). As in the case of the above mentioned DINEOF applications, spatial locations with more than a 95% of missing data are not included in the DINEOF reconstruction procedure to prevent a negative impact on the quality of the overall reconstruction. The covariance filtering option proposed in Alvera-Azcárate et al. (2009) was also applied setting the number of iterations of the filter to 12. The number of retained EOFs was high for all experiments (a minimum of 75) independently of the considered gap scenario (see Sec. 4).

3.2 SOM

Here a new methodology has been developed in order to reconstruct HF radar velocity fields in the statistical framework of the Self-Organizing Maps (SOM) analysis. SOM, is a powerful visualization technique based on an unsupervised learning neural network, which is especially suited to extract patterns in large datasets (Kohonen, 1982, 1997). SOM is a nonlinear mapping implementation method that reduces the high dimensional feature space of the input data to a lower dimensional (usually two dimensional) network of units called neurons. In this way, SOM is able to compress the information contained in a large amount of data in a single set of maps. The learning process algorithm consists in a presentation of the input data to a preselected neuronal network, which is modified during an iterative process. Each neuron (or unit) is represented by a weight vector with the number of components equal to the dimension of the input sample data. In each iteration the neuron whose weight vector is closest (more similar) to the presented sample input data vector, called Best-Matching Unit (BMU), is updated together with its topological neighbors located at a distance less than the neighborhood radius R_n towards the input sample through a neighborhood function (see Hernández-Carrasco and Orfila, 2018b for a schematic representation of the SOM). Therefore, the resulting patterns will exhibit some similarity because the SOM process assumes that a single sample of data (input vector) contributes to the creation of more than one pattern, as the whole neighborhood around the best matching pattern is also updated in each step of training. It also results in a more detailed assimilation of particular features appearing on neighboring patterns, if the information from the original data enables to do so. At the end of the training process, the probability density function of the input data is approximated by the SOM and each unit is associated with a reference pattern, with a number of components equal to the number of variables in the dataset, so this process can be interpreted as a local summary or generalization of similar observations.

For typical remote sensing imagery, the SOM can be applied to both space and time domain. Here, since we are interested in the reconstruction of HF currents, we have addressed the analysis in the spatial domain. In this case the input row vector has been built using the radial velocities maps at each time, so each neuron corresponds to a characteristic radial velocities spatial

pattern over the coverage area of the HFR. Since each step iteration has associated a time and location of the sample, we can obtain the time of a particular spatial pattern computing the BMU for each time, providing a time series of the corresponding spatial pattern.

From these ideas, we can deduce the following simple algorithm for reconstructing missing values in the HFR velocity field from the available HFR data:

(i) *Initialization*: Set up of the initial neural network. Each neuron (or SOM unit) has associated a weight vector, W, composed of random values of HFR radial velocities (called Random initialization).

(ii) *Training process*: Radial HFR velocities values at a time t_i (Map of HFR velocities, $U(\mathbf{x},t_i)$) are used as input vectors, $V_i=U(\mathbf{x},t_i)$, to iteratively feed the neural network. This process is divided in two phases: a rough training using a larger neighborhood radius R_n in the neighboring function and a finetune training for small R_n. Note that V_i are the HFR velocity maps with missing points.

(iii) *Spatial patterns:* Once the training process has finished we obtain an ordered neural network of spatial patterns of radial HFR velocities (V_s). Now V_s does not include missing values.

(iv) *Identification of missing values (NaNs):* Locate the position and time of the HFR velocity grid points with missing values ($\mathbf{x}_m,t_m$).

(v) *Find BMU:* Identify the most similar SOM spatial pattern to the HFR radial velocity map with missing values ($BMU(V_i(\mathbf{x}_m,t_m))$).

(vi) *Replace missing values:* Once we have assigned the BMU we replace the points with missing values with values of the corresponding grid point of the BMU, obtaining the filled HFR velocity field, V_f, where

$$V_f(\mathbf{x},t) = BMU(V_i(\mathbf{x}_m,t_m)) \qquad \forall(\mathbf{x},t), U(\mathbf{x},t) = NaN \tag{1}$$

$$V_f(\mathbf{x},t) = V_i(\mathbf{x},t) \qquad \forall(\mathbf{x},t), U(\mathbf{x},t) \neq NaN \tag{2}$$

(vii) *Replace all NaNs:* Repeat (v) and (vi) for all the points with missing values.

The ability of this method relies on the precision of identifying the proper BMU that describes accurately the missing dynamics. We try to optimize the algorithm by using as input vector a concatenation of three maps of HFR velocities at three different dates. Thus we force the method to distinguish between three maps instead of one, avoiding the selection of a bad BMU, in particular when the HFR velocity map has a large number of missing points at time t_0 and there are not enough number of points to compare with the SOM patterns. The input vector is thus $V_i=[U(\mathbf{x},t_0-\Delta t),U(\mathbf{x},t_0),U(\mathbf{x},t_0+\Delta t)]$. We have checked different values of Δt and we have found the best results when using $\Delta t = 4$ hours.

Initialization, training process and final output of the SOM algorithm have to be tuned up in order to optimize the results and the computational cost by selecting particular control parameters. For instance, the optimal size of the neural network (number of neurons) depends on the number of samples and on the complexity of the patterns to be analyzed. We choose the map size as

[50 x 50], with 2500 neurons. Using different sizes, for instance, [100 x 100], the spatial patterns are more detailed and more variability of patterns emerges. However, these new patterns make it difficult to find the proper BMUs for the specific date providing considerable problems to accurately reconstruct the desired field in the missing points. The opposite happens using a reduced number of neurons, patterns are concentrated together in few rough neurons without discriminating regions with differ-
5   ent dynamical processes. We use hexagonal map lattice to have equidistant neighbors and do not introduce anisotropy artifacts. Concerning to the initialization, we opted for random mode. There are other initializations, i.e. based on linear combination of the EOFs modes of the HFR velocities, but all of them yield similar results. We choose random initialization since it is faster as well as missing data are accepted. For the training process we use the imputation batch training algorithm (Vatanen et al., 2015) adapted for data with missing values, and 'gaussian' type neighborhood function since this parameter configuration produces
10   a good compromise between quantitative and topological error and computational cost (Liu et al., 2006). The neighborhood radius is chosen to vary from 20 to 0.1. Other values of the neighborhood radius have been tested without improving the results with the same computational cost. These SOM computations have been performed using the MATLAB toolbox of SOM v.2.0 Vesanto et al. (2000) provided by the Helsinki University of Technology (http://www.cis.hut.fi/somtoolbox/).

Comparing with the conventional statistical methods like the EOF and K-means, SOM is able to introduce nonlinear corre-
15   lations and it does not require any particular functional relationship or distribution assumptions about the data, i.e., distribution normality or equality of the variance (Liu et al., 2006, 2016). SOM has been applied in a wide range of scientific disciplines. Among others, it has been used in climate sciences (Cavazos et al., 2002), in genetics, working with DNA sequences (Nikkilä et al., 2002), or ecological sciences applications (Chon, 2011). In the physical and biological oceanography context SOM has also been used in several studies (Richardson et al., 2003; Liu and Weisberg, 2005; Hales et al., 2012; Charantonis et al., 2015;
20   Liu et al., 2016; Hernández-Carrasco and Orfila, 2018b; Basterretxea et al., 2018). However, to our knowledge, applications of SOM analysis on the reconstruction of HF radar velocity fields have not been addressed.

4   Experiments: Catalog of HFR Gaps

The most common real scenarios for spatial gaps in HFR data are mainly represented by individual antenna failures, range and/or bearing reduction. The radio signal emitted by an HFR travels along and back through the ocean surface due to the
25   conductivity of the ocean and the currents velocity is measured based on the Bragg scattering phenomena (Barrick et al., 1977) of the received signal. Any affection to this process will result in gaps in the final data. Among the most common reasons to find spatio-temporal data gaps in radial (and total) components are adverse environmental conditions and/or electromagnetic problems as the lack of Bragg scattering ocean waves, severe ocean wave conditions, the occurrence of radio interference or changes of the electromagnetic field in the vicinity of the antennas which lead to invalid antenna patterns and calibration
30   parameters. Additionally there is a permanent region between the antennas, the so-called baseline, where the total currents cannot be computed in an accurate way. The baseline between two HFR sites is defined as the area where the radial components from the two sites have an angle of less than 30°, so the total velocity vectors created from radial data within this area contain greater uncertainties. Normally, the solution in the baseline is not computed, so we observe a data gap in an area which is

delimited by the rule of geometric dilution of precision (GDOP) (Barrick, 2002; Chapman et al.) and the limits set to this quality control parameter in the processing of the data from radials to totals. The permanent spatial gap in the baseline is an issue than can be problematic for the assessment of the dynamics near the coastal area between the antennas.

In order to characterize the most typical and realistic gap types observed in the Basque HFR system, K-means classification algorithm (Hastie et al., 2009), henceforth KMA, is applied to the real radial data for 2014. Before applying the KMA, the radial data are converted to 1 or 0 values, depending on the availability or absence of data for each radial position, respectively. Then KMA is used to classify the dataset into a specified number of groups according to the similarity in the distribution of gaps exhibited in the HFR data set (Hastie et al., 2009). The selection of the number of groups is done qualitatively, as proposed by Guanche et al. (2014). In our case we choose to keep 16 groups since this number facilitates the interpretation of the gap scenarios without loosing variability of the data set (Figure S1 in supplementary material). Groups 1, 5, 8, 9, 10, 14 and 15 are considered to represent a good data coverage; groups 4, 6, 7, 11 and 13 contain most of the common scenarios of spatial data-gap; and finally, groups 2, 3, 12 and 16 show situations with no (or very few) data for any of the two antennas (no total currents can be produced). Examples of good coverage and gap scenarios corresponding to individual antenna failure, range reduction and bearing are shown in Figure 2.

Since the goal of this work is to evaluate different gap-filling methodologies in real situations, the different groups representing observed gap types are used to introduce artificial gaps in April 2012, April 2013 and April 2014. Besides, randomly generated spatial gaps are also included to cover different failures that are not related to the typical situations but could occur. For all the cases data gaps are introduced in 50% of the time series. The proposed gap scenarios are: (A) Bearing gaps, generated by randomly distributing 10 of the elements of KMA group 6 (Figure 2); (B) Decreasing range generated by randomly distributing 10 of the elements of KMA group 4; (C) Antenna failure: in this group failures of one of the two antennas were simulated by randomly removing data from one of the sites; (D) Random gaps: gaps were randomly introduced in the time series and randomly distributed over 30% of the spatial HFR domain. K-means analysis shows that the situation associated to the patterns with a percentage of gaps greater than a 30% is likely due to a failure of one of the two antennas than to other causes. This last scenario represents a situation where data in selected locations has been removed (for instance after a quality control procedure based on a velocity or variance threshold, as recommended by the QARTOD manual, IOOS 2015). Figures 3 and 4 show the temporal and spatial distribution of the percentage of coverage of the original data and the new dataset generated by introducing the previously described gaps to the original data.

These gap scenarios (from now on referred as experiment A, B, C and D) are used to test the SOM, DINEOF and OMA gap-filling methodologies. For OMA, total maps are generated using OMA directly on radial data. For DINEOF and SOM, hourly radials are gap-filled first and then totals are generated using the same least mean square algorithm (spatial interpolation radius of 10 km) used to build the reference data series (i.e. from the reference radial files with no gaps).

4.1 Definitions and statistical metrics used for the filled-original currents comparison

In this study we compute different Lagrangian quantities using the HFR velocity field filled by the three different methods explained in Section 3: SOM, DINEOF and OMA. All the Lagrangian quantities, F (finite size Lyapunov exponents -FSLE-
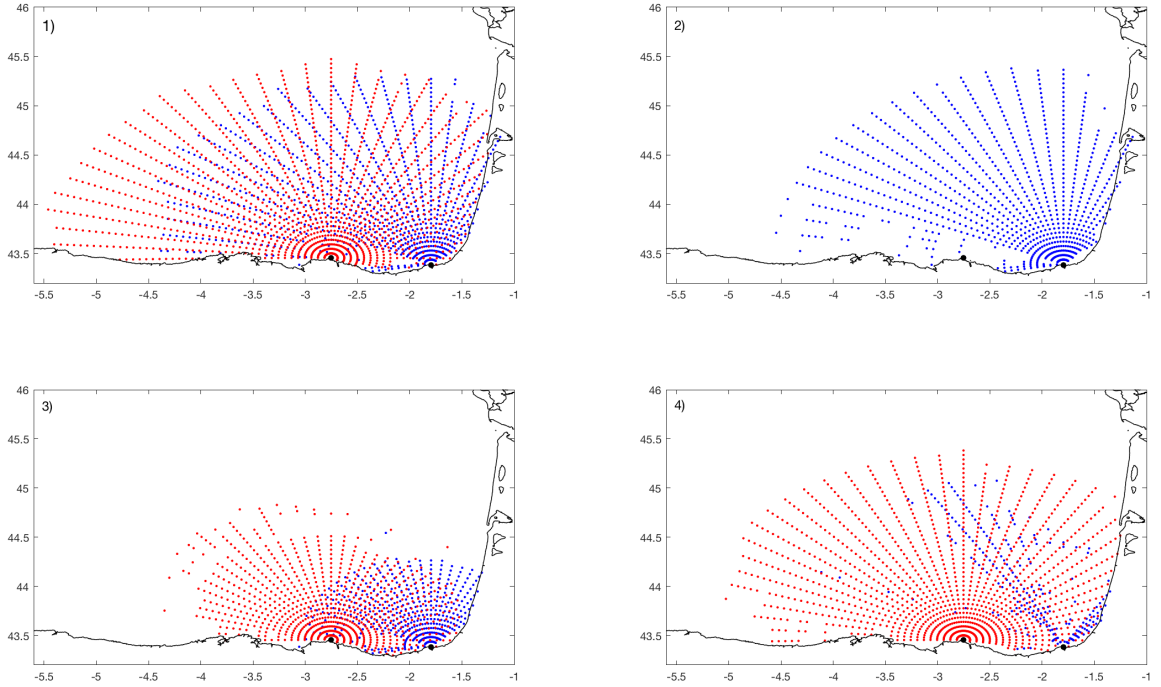
Figure 2. Example of the four prototypes of KMA groups of gap distribution scenarios obtained from the KMA analysis applied to HFR availability-absence matrix for 2014. (1) representing a good data coverage scenario. (2) accounting for the failure of one of the two antennas. (3) characterizing a range decrease in both antennas. (4) representing bearing coverage decreasing in one of the antennas. Matxitxako radials are plotted in red and Higer radials are plotted in blue. (See figure S1 in supplementary material for the complete KMA results lattice).

and residence times -RT-), computed from SOM are referred as SOM-F. For instance if we compute the FSLE from the SOM reconstructed HFR currents, it is referred as SOM-FSLE. The same for DINEOF and OMA. We use as the reference field the original HFR velocity field in the periods when it is complete. This complete HFR data set is named REF, and, for instance, REF-FSLE refers to FSLE computed from REF.

5   We use conventional statistical metrics to measure differences between gap-filled and observation data to quantify methodology skill: absolute relative error (ARE), mean bias (MB), and root mean squared error (RMS). Denoting a set of reference observational values as R, corresponding data obtained from the filled velocity field as G, using brackets to denote the mean of the set, and a prime to denote variations from the mean, i.e., $G'=G-<G>$, these error metrics are defined as:
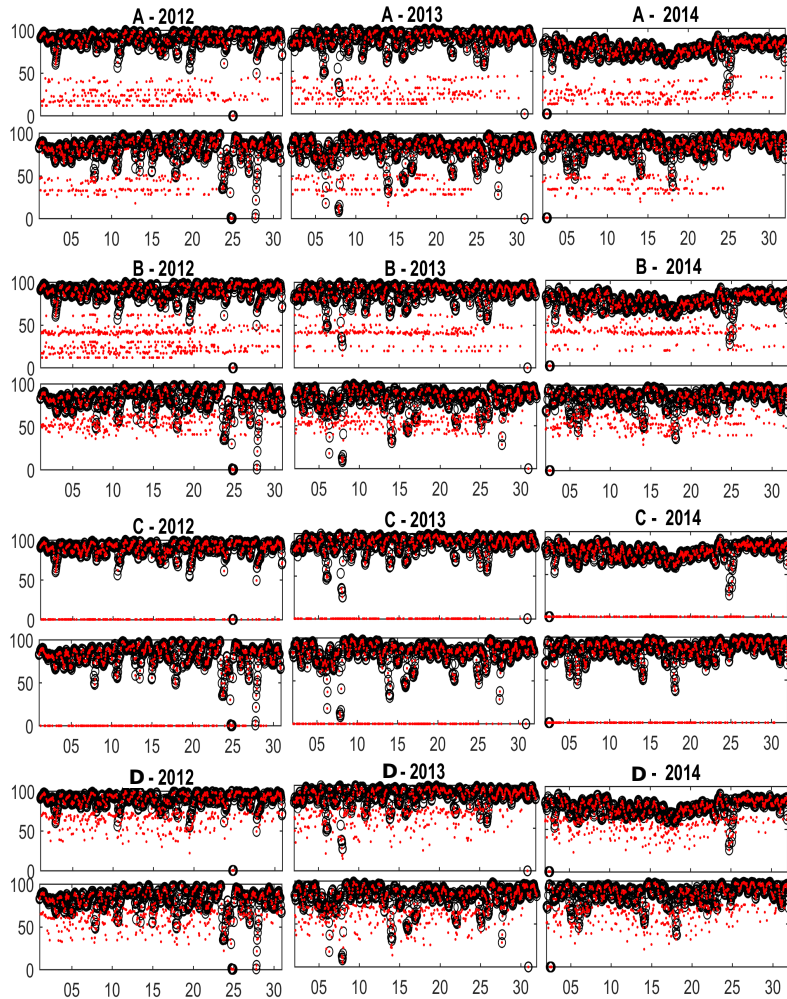
Figure 3. Percentage of spatial coverage for each time step and experiment. Higer data is shown in the upper panels and Matxitxako data in the lower panels in all cases. Black circles represent the percentage of good data for the original fields. Red dots denote the percentage of good data for each experiment. X-axis is the time step of the time series for April 2012, April 2013, April 2014.

$$ARE = \frac{1}{N} \sum_{i=1}^{N} \left| \frac{G(i) - R(i)}{R(i)} \right|, \tag{3}$$

$$MB = \frac{1}{N} \sum_{i=1}^{N} (G'(i) - R'(i)), \tag{4}$$

$$RMS = \frac{1}{N} \sum_{i=1}^{N} (G(i) - R(i))^2, \tag{5}$$
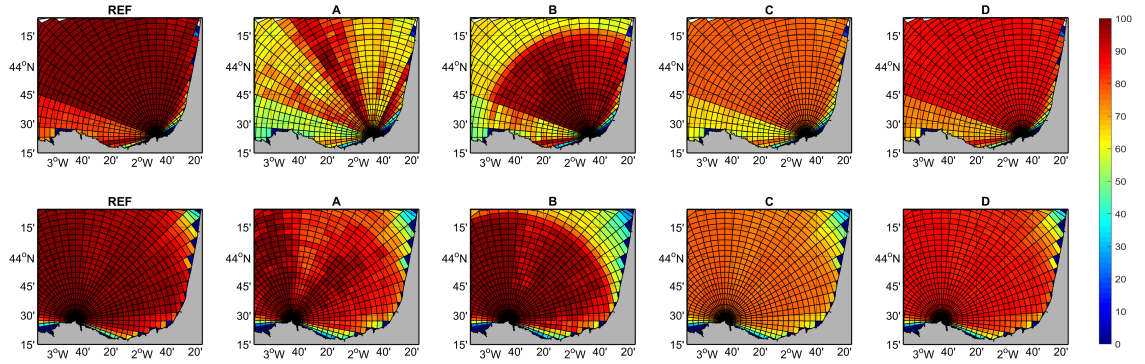
Figure 4. Maps of temporal coverage (percent of the total number of hours in the 3-month period analyzed) for Higer (upper panels) and Matxitxako (lower panels), for the REF series and all the experiments.

where N is the number of pixels in the velocity field.

5 Results

5.1 Eulerian Comparison

Scatter plots of zonal (u) and meridional (v) velocities reconstructed by the three models versus the reference field and for the
5 four experiments are shown in Figure 5 and Figure 6, respectively. In the case of OMA the cloud of points is, in general, wider with more points separated from the baseline. In general the behavior of SOM and DINEOF methods is very similar in terms of RMS, BIAS and R^2 as displayed in Tables 1 and 2 for the u and for the v component of the velocity, respectively. Although SOM tends to underestimate currents and DINEOF to overestimate, OMA is showing the worst reconstruction, specially for experiment C. It is worth to note that models behave similarly for component u and component v for all experiments. The
10 lowest mean error is found for experiment D with values of 0.36, 0.35 and 0.38 for SOM, DINEOF and OMA, respectively, and the highest for experiment C with values of 0.43, 0.38 and 0.57 for SOM, DINEOF and OMA, being the antenna failure the worst-case gap scenario to be properly reconstructed. In particular, the scatter plot of reference *vs.* reconstructed zonal velocities from DINEOF in the case of the experiment C (Figure 5 second column, third row) shows many points out of the main cloud. It suggests that the gap scenario C, where a very small number of observations is available (failure of one antenna),
15 is the most difficult gap scenario for the DINEOF methodology. Typically a 5% minimum threshold of available data is used in most DINEOF applications reported in the literature to accept a candidate for a potential reconstruction (for instance, a gappy satellite image, an hourly HFR current field, etc.). As described in Sec 3, such a threshold is also applied here as a pre-processing step before the technique is applied. The spatial field of the missing antenna is reconstructed using available data from the other antenna, as well as using data from previous and subsequent time steps. Although, in general, the field might be

acceptably reconstructed, it seems that some parts of the HFR image are not properly reconstructed. This result suggests that DINEOF should not be considered in situations represented in the scenario C, especially when the antenna failure is persistent over time. Relative errors are slightly lower for DINEOF than for SOM but with more outliers as shown in Figures 5 and 6.
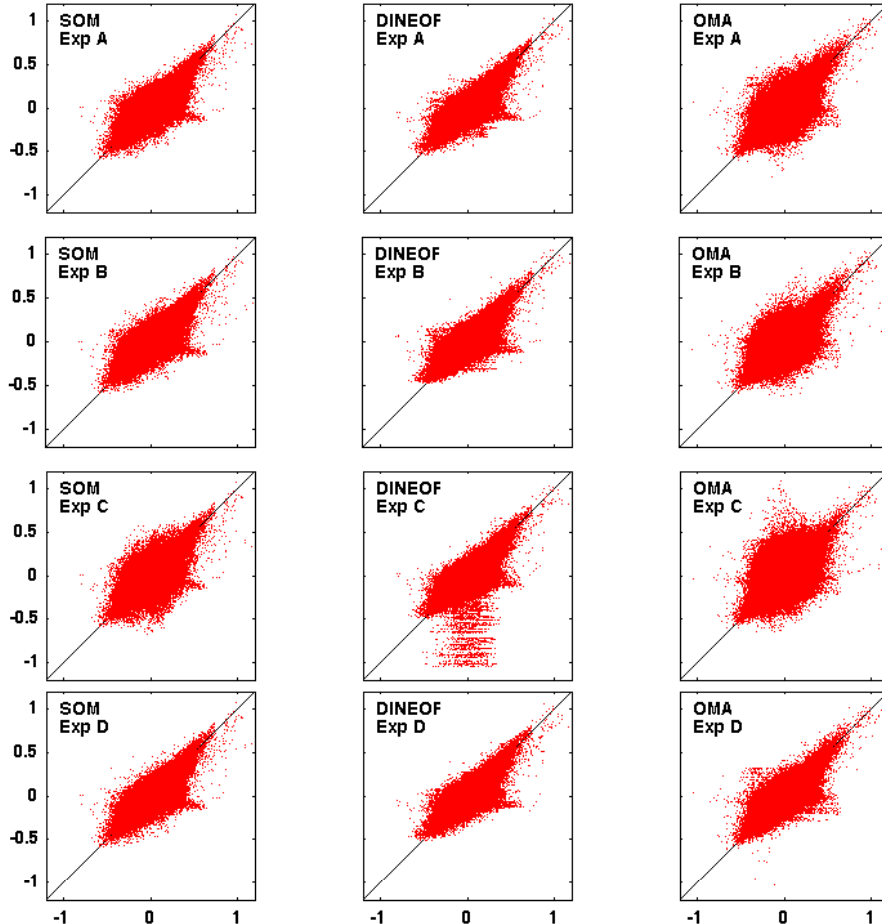
Figure 5. Scatter plot of the SOM (first column), DINEOF (second column) and OMA (third column) reconstructed zonal velocities *vs* observations for the four experiments (rows).

5.2 Comparison of trajectories

5 Synthetic trajectories are computed advecting particles in the original HFR velocity field (reference trajectories) and also in the OMA, SOM and DINEOF gap-filled currents. A total of 868 particles are initially uniformly distributed over the HF radar grid with a initial distance between particles of 5 km. Lagrangian particles are released every hour from the 2nd to the 26th of April 2012, 2013 and 2014 and advected during 72 hours. Trajectories are computed using a fourth-order Runge-Kutta

Table 1. Root Mean Square Error (RMS), Mean Bias (MB) and Correlation Coefficient (R^2) of the zonal velocities (u) obtained using reconstructed HFR field from the three methodologies and for the four experiments with respect to the zonal velocities derived from the Reference HFR currents

		SOM	DINEOF	OMA
Experiment A	RMS (m s^{-1})	0.0620	0.0558	0.0732
	MB (m s^{-1})	-0.0021	0.0011	-0.0006
	R^2	0.8703	0.8959	0.8239
Experiment B	RMS (m s^{-1})	0.0609	0.0588	0.0747
	MB (m s^{-1})	-0.0013	0.0014	0.0000
	R^2	0.8753	0.8830	0.8145
Experiment C	RMS (m s^{-1})	0.0712	0.0648	0.0938
	MB (m s^{-1})	-0.0019	-0.0001	0.0071
	R^2	0.8300	0.8604	0.7158
Experiment D	RMS (m s^{-1})	0.0585	0.0553	0.0599
	MB (m s^{-1})	-0.0017	0.0016	-0.0006
	R^2	0.8847	0.8976	0.8805

integration scheme and a bilinear interpolation of the gridded velocity field in space and linear in time. The mean distance of separation (D) between particle trajectories advected by the reference velocity field and by the reconstructed current fields averaged over all pairs of trajectories is plotted against time for each experiment in Figure 7. After 10-15 hours, differences in D start to be visible in all the cases. In all the experiments, DINEOF and SOM show lower separation distances and a similar behavior, while OMA method is the one showing the highest errors, in particular in the case of failure of one of the antennas (Experiment C). In this case OMA capability to fill gaps is limited (as discussed in Kaplan and Lekien, 2007) and the effects can be noticed from the beginning of the trajectory simulation. DINEOF and SOM methods show similar results, with separation distances around 1 km after 24 hours of simulation and 3 km after 72 hours. Values of D for SOM are slightly smaller, in all of the experiments. On the contrary, this distance reaches values of 5 km after 24 hours in the case of OMA. The values of D obtained in our computations after 24 hours of simulation are smaller than those reported in Molcard et al. (2009); Bellomo et al. (2015); Kalampokis et al. (2016) for separation distances between real and virtual drifters trajectories. It is important to keep in mind that in these experiments the trajectories are calculated with data from different sources (HFR and drifters) and different sampling (spatial resolution) which are collected in a different region (Mediterranean Sea). However, the fact that we

Table 2. Root Mean Square Error (RMS), Mean Bias (MB) and Correlation Coefficient (CC) of the meridional velocities (v) obtained using reconstructed HFR datasets from the three methodologies and for the four experiments with respect to the zonal velocities derived from the Reference HFR currents

		SOM	DINEOF	OMA
Experiment A	RMS (m s^{-1})	0.0547	0.0499	0.0608
	MB (m s^{-1})	0.0023	0.0022	-0.0018
	R^2	0.8839	0.9031	0.8547
Experiment B	RMS (m s^{-1})	0.0519	0.0508	0.0579
	MB (m s^{-1})	0.0016	0.0023	-0.0022
	R^2	0.8966	0.8992	0.8668
Experiment C	RMS (m s^{-1})	0.0619	0.0540	0.0806
	MB (m s^{-1})	0.0020	0.0030	-0.0023
	R^2	0.8499	0.8864	0.7510
Experiment D	RMS (m s^{-1})	0.0515	0.0501	0.0518
	MB (m s^{-1})	0.0017	0.0023	-0.0011
	R^2	0.8970	0.9027	0.8925

obtain smaller values of D is an indication of the high performance of the three methods, with better results observed for the SOM method as compared with OMA and DINEOF.

The spatial distribution of separation distances between real and simulated trajectories has also been analyzed in order to detect any anisotropy in the differences between them (Figure 8). The results show the same behavior of the temporal separation distances between the different methodologies and experiments, but DINEOF and SOM yield better results than OMA. It is worth to note that OMA capability decreases in the half west part of the study area in all the experiments and specially when there is a failure in one of the two antennas (Experiment C). It is also noticeable that the time average of the separation distances are smaller in this experiment for DINEOF than for SOM. In general, all the methodologies show lower separation distances in the central and eastern part of the study area than in the western part which demonstrates that the performance of the methodologies has spatial variations and is not uniform.
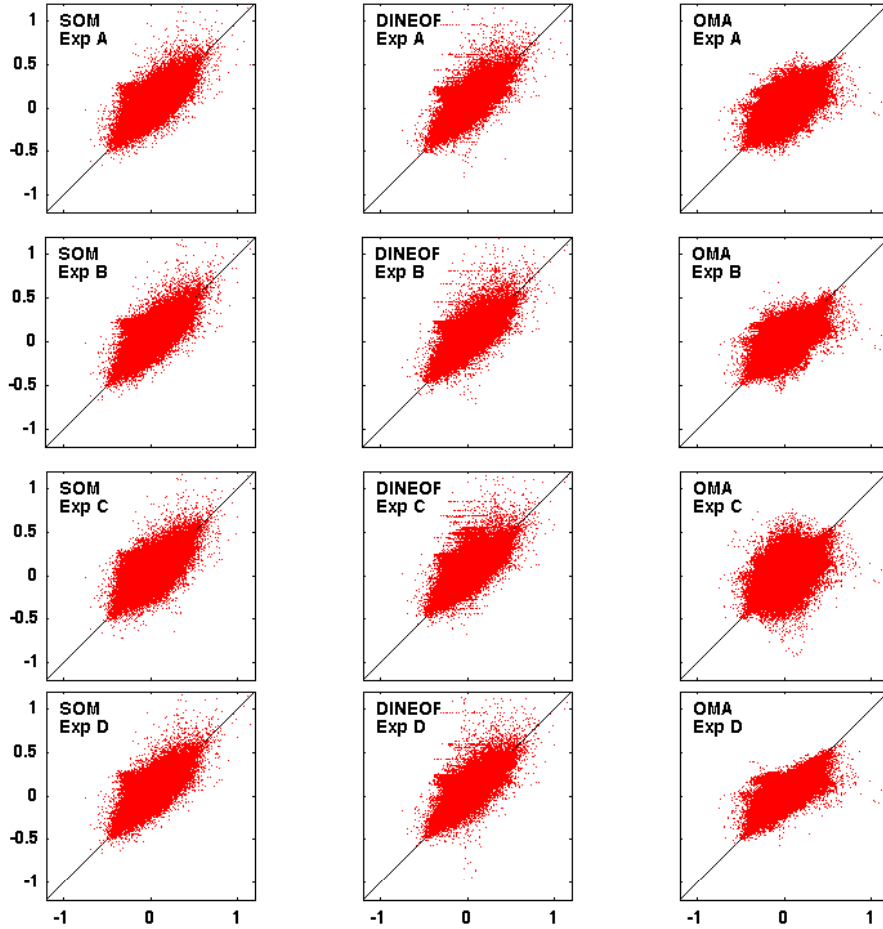
Figure 6. Scatter plot of the SOM model (first column), DINEOF (second column) and OMA (third column) reconstructed meridional velocities *vs* observations for the 4 experiments (rows).

5.3 Lateral stirring analysis

Furthermore, we analyze the effect of the different gap-filling methodologies on the FSLEs computations. FSLE was originally introduced in the dynamical system theory to characterize the growth of non-infinitesimal perturbations in turbulence (Aurell et al., 1997) and to characterize flows with multiple spatio-temporal scales (Boffetta et al., 2000; Lacorata et al., 2001). In addition, FSLE can be used to unveil dynamical structures, called Lagrangian Coherent Structures, LCS, identifying fronts, eddies, jets, (Hernández-Carrasco et al., 2011), as well as to study the flow stretching and contraction properties in geophysical data (Joseph and Legras, 2002; Lipphardt et al., 2006; Shadden et al., 2009; Hernández-Carrasco et al., 2012).

The contribution of the scales captured by the HFR in the ocean surface dynamics can be analyzed by computing particle dispersion at different spatial scales, δ (Boffetta et al., 2000; Haza et al., 2010; Corrado et al., 2017), using the following
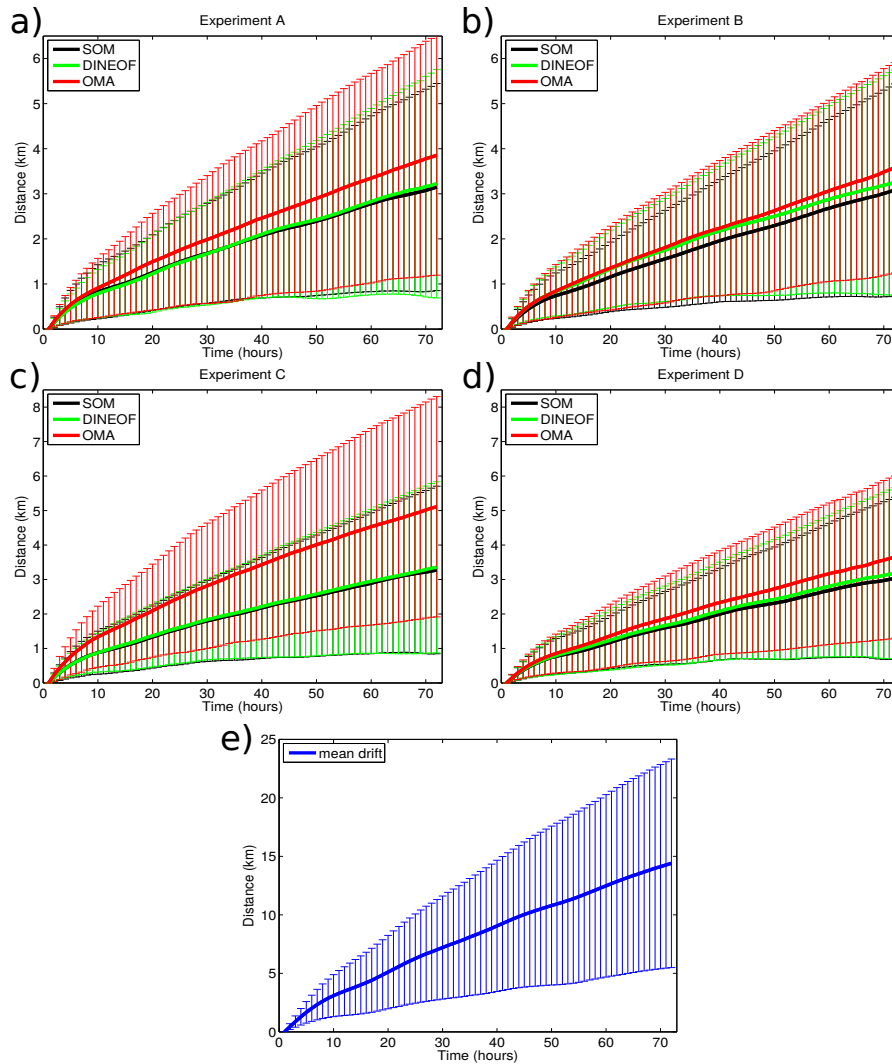
Figure 7. Separation distance between particle trajectories advected by the filled HFR velocity field and by the reference velocity field as a function of time and averaged over all the pairs of trajectories. Different limits in the vertical axis of the figure have been used for a better data representation. The error bar is the confidence interval (one standard deviation) of the spatial average of D(t).

equation for FSLE,

$$\lambda(\delta) = \frac{\ln(r)}{\langle \tau(\delta, r\delta) \rangle}, \tag{6}$$

where $\langle \tau(\delta, r\delta) \rangle$ is the time (τ) needed for the initial perturbation δ (initial pair of particles separation) to grow $r\delta$ averaged over all the pairs of particles for every initial perturbation δ and a fixed threshold rate, r. A small value, $r < 2$, allows capturing the relative dispersion driven by small coherent features, but r should not be close to 1 to avoid aliasing problems associated
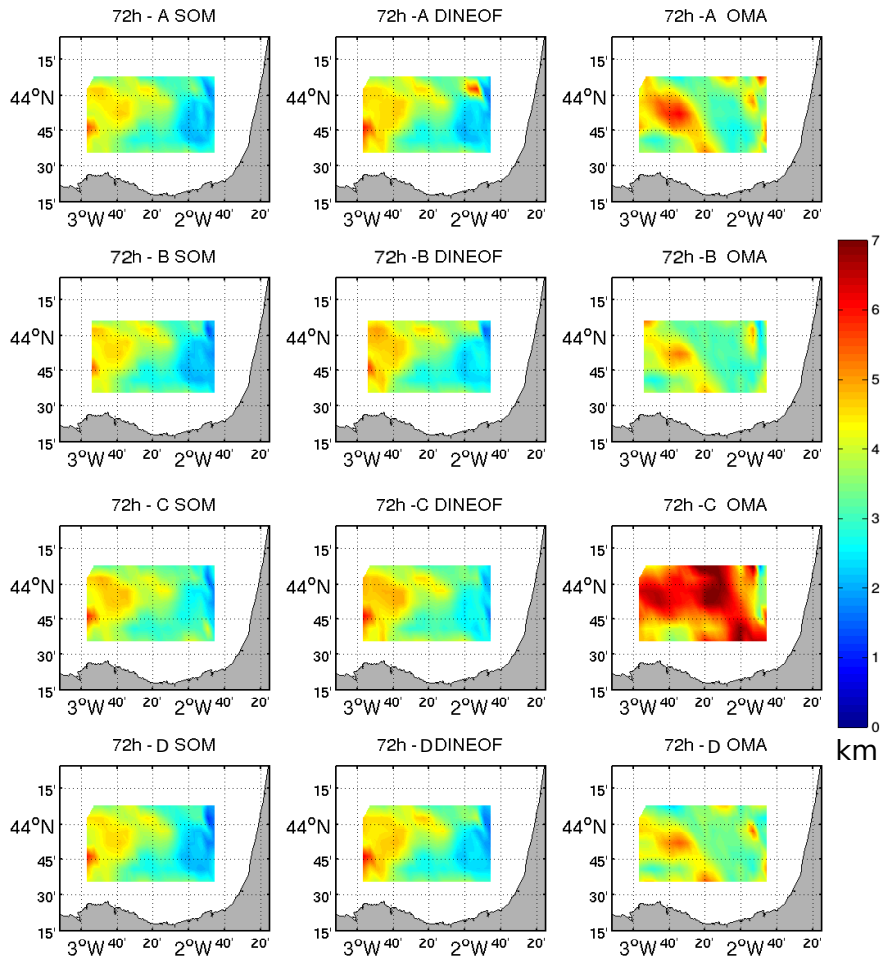
Figure 8. Time average of the separation distance between trajectories computed from the filled HFR using the three methodologies and reference HFR velocities initiated in the same pixel.

with the time step of particle advection at small scales (Lacorata et al., 2001; Haza et al., 2008). FSLE is a measure of relative dispersion where the spatial variable is the independent variable.

We evaluate how the gap-filling methodologies impact on the dynamical scales captured by the HFR. Figure 9 shows the averaged FSLE curves obtained from the three methodologies in two of the four experiments. The other experiments yield similar results. In all of them, $\lambda(\delta)$ is not constant over the range of scales covered by the HFR (scale dependent). In the REF case the best-fitting of the averaged FSLE curve shows a slope of -0.50 and a correlation coefficient, R^2, of 0.97. This indicates that the average scaling law of the relative dispersion over the scales from 6 km to 40 km is associated to a turbulent dispersion for flows with a k^{-2} type of spectrum (Klein et al., 2008; Capet et al., 2008), suggesting that ageostrophic velocities and
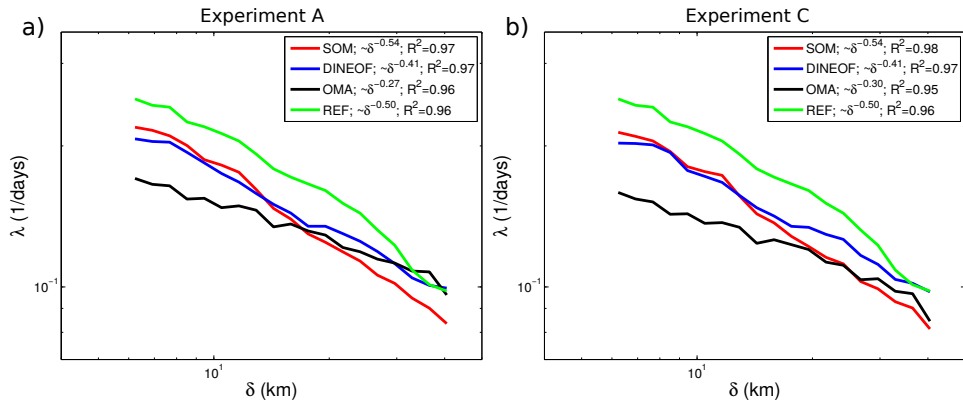
Figure 9. Comparison of scale-dependent FSLE curves computed from the different filled HFR velocities, averaged over 240 virtual pair of particles deployments homogeneously distributed through April 2012, 2013, 2014. a) experiment A, b) experiment C.

frontogenesis are contributing to the lateral dispersion at these scales (Callies and Ferrari, 2013). This means that the separation rate is controlled by structures with size comparable with the separation itself, therefore the dispersion regime is local. The slope of the FSLE curve derived from the REF HFR velocity field is in agreement with previous modeling studies, with a slope similar to those derived from surface synthetic drifter trajectories integrated by high-resolution numerical simulations (Choi
5   et al., 2017). It further reinforces the fact that the velocity field of the HFR is adequate to study small-scale dynamics.

Comparing the FSLE slopes obtained from the three gap-filling methodologies with the REF HFR velocity field we find that SOM methodology yields the most similar values, with slopes of -0.54 $\pm$ 1, and a R^2 greater than 0.96 for all the experiments, followed by the DINEOF with slopes of -0.41 $\pm$ 1, and a R^2 also greater than 0.96 for all the experiments. Finally OMA yields the largest differences with slopes comprised between -0.27 and -0.30 and high R^2 (greater than 0.94). The SOM-FSLE slopes
10   are slightly steeper than the REF-FSLE suggesting that this methodology could introduce noise in the reconstruction of the data. On the other hand DINEOF-FSLE slopes are slightly flatter than the REF-FSLE, which could be produced because this methodology smooths the velocity field or because it favors larger scales as captured by EOFs. However OMA-FSLE slopes are clearly flatter than the REF-FSLE. In this case, $\lambda(\delta)$ is almost constant over the range of scales (scale independent), the separation of particles is almost exponential with a constant rate and we have a nearly exponential regime. In this regime the
15   relative dispersion is non-local, indicating that not only the small scale processes govern the dispersion but also the larger structures. This result suggests that OMA has a strong smoothing character, removing small features from the velocity field, as reported in previous Eulerian studies (Kaplan and Lekien, 2007).

Comparing with other observational studies using HFR the λ obtained from our computations is one order of magnitude smaller than the one reported in Haza et al. (2010) (λ= 4 to 7 days^{-1} for $\delta < 1$ km) computed from VHF Radar with 300 m
20   of spatial resolution in the Gulf of La Spezia. This is expected when comparing their scales of interest [0.1 - 1km] against our range of resolved scales [5 - 25 km](Corrado et al., 2017). Hernández-Carrasco et al. (2018), using HFR velocities at 3 km of resolution in the Ibiza Channel, reported larger values of λ (between 0.6 and 0.2 days^{-1}) at spatial scales between 3 and
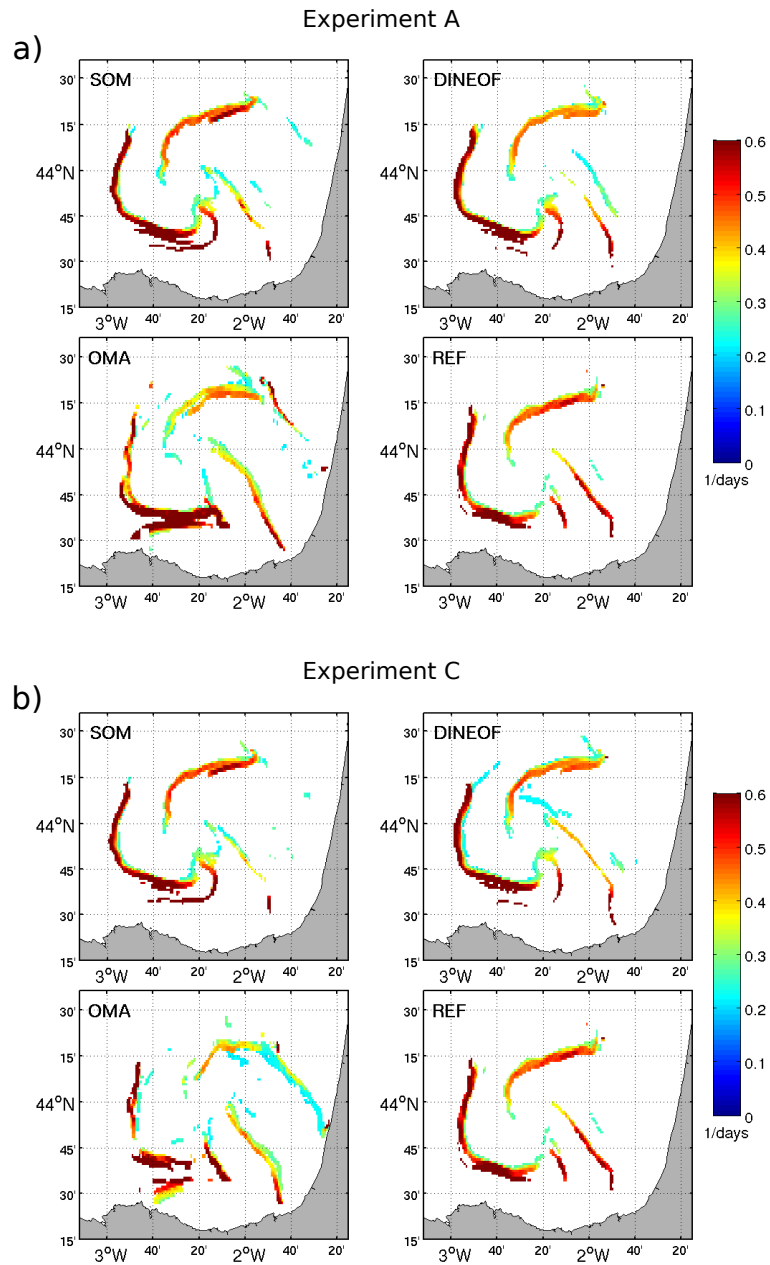
Figure 10. Snapshots of attracting LCS computed from the three filled and the reference HFR currents for the experiment A (a) and experiment C (b) corresponding to April 11, 2014, 00:00.

30 km following a Richardson slope. Other studies based on drifters in the Gulf Stream (Lumpkin and Elipot, 2010) or in the Gulf of Mexico (Poje et al., 2014) or in the Mediterranean Sea (Schroeder et al., 2011; Griffa et al., 2013) have found higher
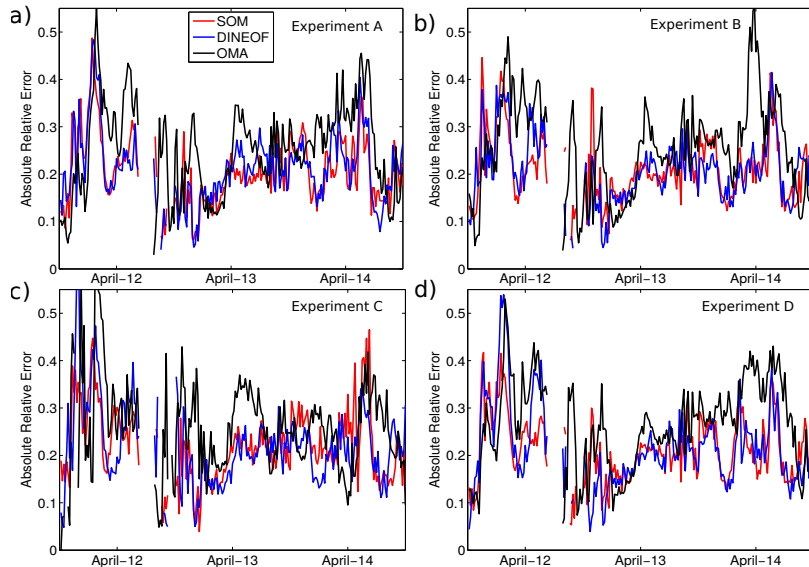
Figure 11. Time series of the spatial average of the pixel by pixel absolute relative error of the LCS computed from the three filled HFR velocities with respect to LCS obtained from the reference velocity field.

.

values of $\lambda(\delta)$ at these scales. Regional differences as well as possible observational biases could explain these discrepancies in FSLE values. For instance, differences in the topographic boundaries, the presence of coastal jets, tidal currents, particular wind regimes, etc, can influence the dynamics affecting the transport processes at the coastal sea surface.

In general the λ obtained for the three methodologies and for all the experiments are smaller than for REF, in particular when
5   OMA velocities are used. At the smallest scales studied here (5-15 km) SOM-FSLE is the most similar and at larger scales DINEOF-FSLE and OMA-FSLE values are closer to REF-FSLE.

Next we analyze the effect of the reconstructed velocities on the LCS. FSLE is used to obtain the LCS by computing the minimum growth time of pair-particles separations from δ to $r\delta$ among the four neighbors for each position in order to obtain a FSLE map. In this case, r has to take large values ($r \gg 2$) to adequately distinguish regions of extrema in the FSLE field.
10   Note that in this case the average over the pair of particles in Eq. 6 is omitted.

First we compare some snapshots of the LCS derived from the three reconstructed HFR in order to see differences in the dynamical structures (Fig. 10). We only show LCS from two experiments, A and C, since the results obtained in the experiments B, and D are similar to those of the experiment A. The computed Lagrangian flow structures look rather the same in the case of SOM and DINEOF, despite the large number of missing points reconstructed in both experiments. This is
15   also confirmed by computing the histograms of the FSLE (not shown), which turn out very similar. This is likely due to the averaging process along trajectories performed to compute the FSLE which tends to remove possible errors introduced in the reconstructed velocity fields (Hernández-Carrasco et al., 2011). FSLE is robust against the gaps in the HFR velocity field. On
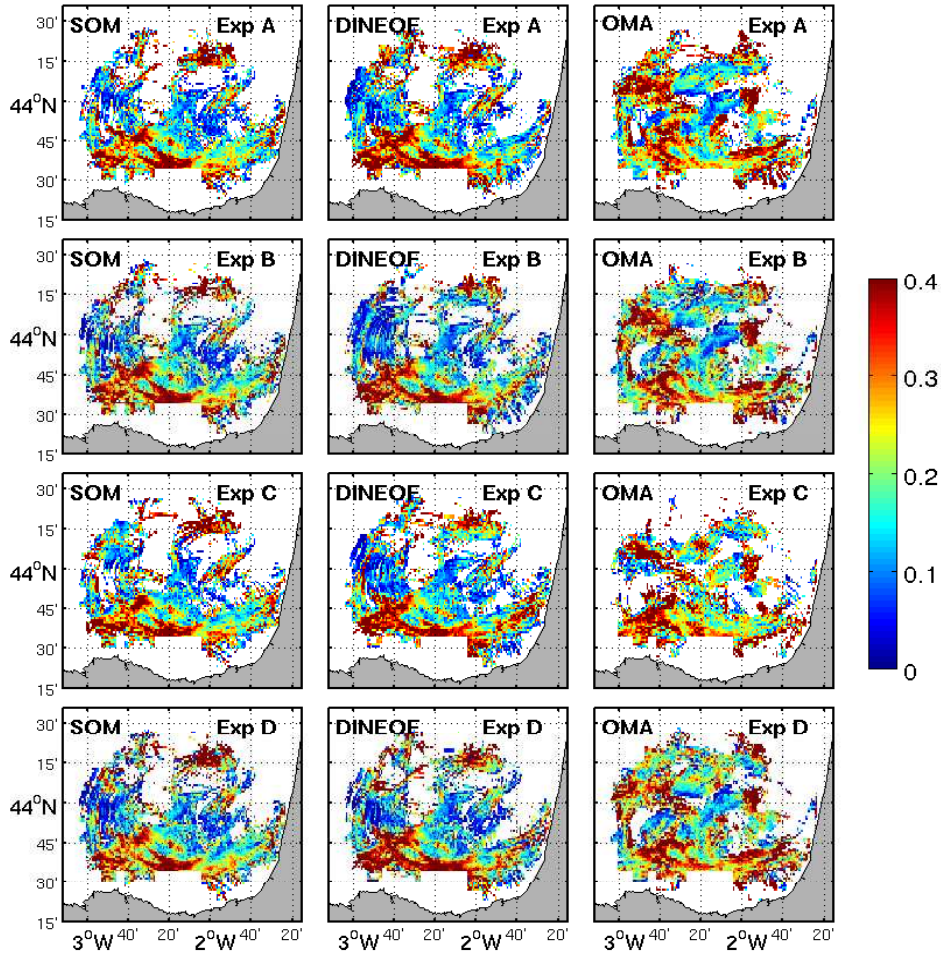
Figure 12. Maps of the time average of the pixel by pixel absolute relative error of the LCS computed from the three filled velocity field with respect to LCS obtained from the reference currents. White color denotes points where LCSs have not been identified.

the other hand OMA is the most affected methodology regarding LCS computations. Even if not very different, one can see some discrepancies in the shape as well as in the location of OMA-LCS with respect to the REF-LCS, as happens in experiment C (Figure 10 b).

Time evolution of the spatial average over the HFR domain of the Absolute Relative Error (ARE, Sec 4.1) of the attracting
5 LCS computed from the reconstructed velocity fields with respect to the REF-LCS is plotted in Figure 11. A common characteristic for the three methods is the large values of ARE during early April 2012 and middle April 2014 for all the experiments, in agreement with the time periods with the largest number of missing values. Comparing the methods one can see that the relative error is mostly greater for the case of OMA and for all the experiments, in particular during the second half of April 2012

Table 3. Mean absolute relative error (ARE) and Mean bias (MB) of the LCS obtained using reconstructed HFR velocities from the three methodologies with respect to the REF-LCS for the four experiments.

		SOM	DINEOF	OMA
Experiment A	ARE	0.20	0.21	0.25
	MB (days^1)	0.01	0.02	$4\cdot10^{-4}$
Experiment B	ARE	0.21	0.21	0.25
	MB (days^1)	0.01	0.01	0.01
Experiment C	ARE	0.22	0.22	0.27
	MB (days^1)	0.01	0.02	-0.02
Experiment D	ARE	0.21	0.22	0.26
	MB (days^1)	0.02	0.03	0.001

and the middle of April 2013 and 2014. All the methods are more affected by the antenna failure simulated in the experiment C, in accordance with the Eulerian comparison.

Further analysis is addressed performing a regional characterization of the impact of the gap-filling methods on the LCS looking at the spatial distribution of the time averaged values of ARE (Fig. 12). One can appreciate that points with accumulated large errors are located in the same regions for SOM and DINEOF, i.e. in the southern area of the BoB HFR domain, and that these regions are the same for the four experiments (near the southern coastline). In addition of possible smoothing or noising, a discrepancy in the location of LCS with respect to the REF-LCS, could explain the large values of the errors. In the case of OMA, additional regions with large errors are distributed all over the BoB HFR domain.

Finally we quantify the difference between the LCS computed from the filled velocities and the REF-LCS computing the spatial and temporal mean of the relative error defined in Eq. 3 and Eq. 4 over all the LCS maps. We summarize in Table 3 the results of these computations. The most significant result is that ARE values are similar for SOM and DINEOF and for all the experiments (around 0.21), being in general slightly smaller for the case of SOM. The largest ARE is found for OMA-LCS, being the experiment C the worst-case gap scenario affecting LCS, with a value of 0.27. The values of MB show that in general the LCS are slightly overestimated. Only in experiment C the values of OMA-LCS are underestimated.

Our results show that even when a large number of pixels is missing the FSLEs still give an accurate picture of the oceanic transport properties and the velocity field filled by the three methods analyzed does not introduce artifacts in the Lagrangian computations.
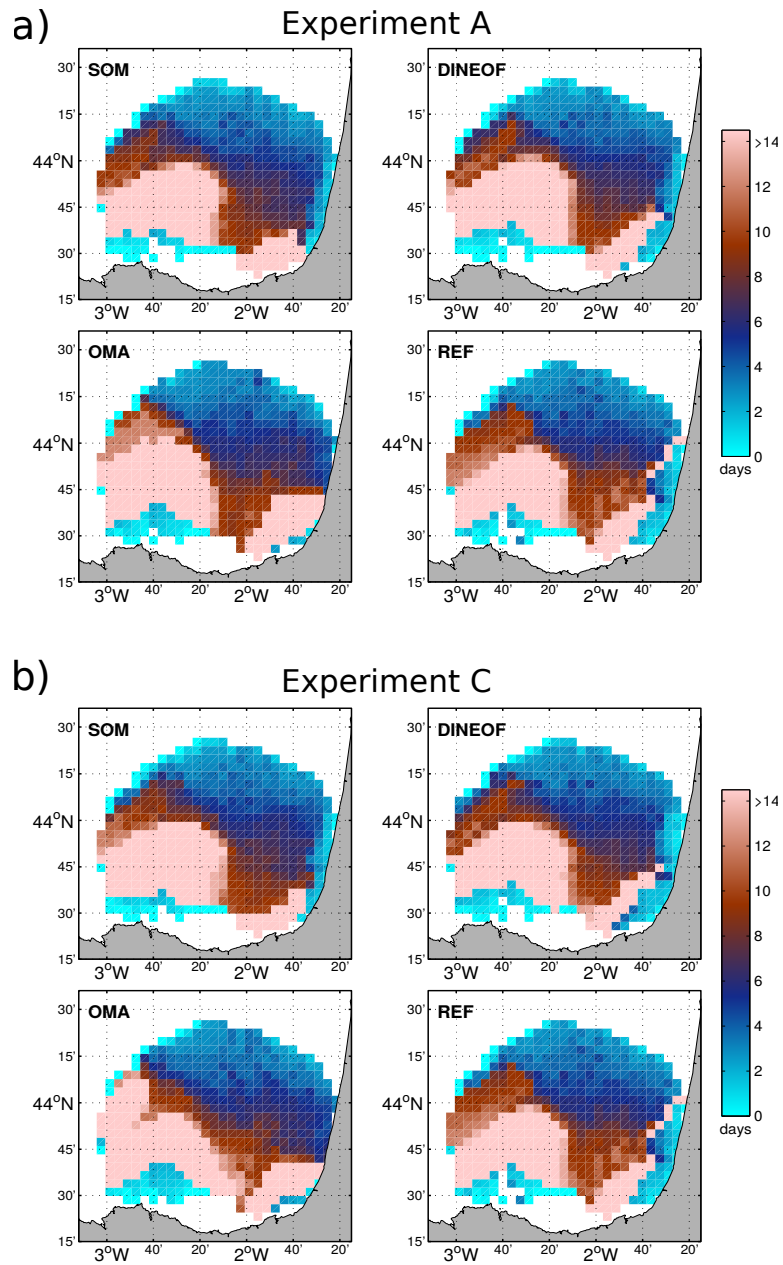
Figure 13. Snapshots of RT computed from the three filled velocity fields and the reference HFR currents for the experiment A and C corresponding to April 04, 2013 18:00.

.
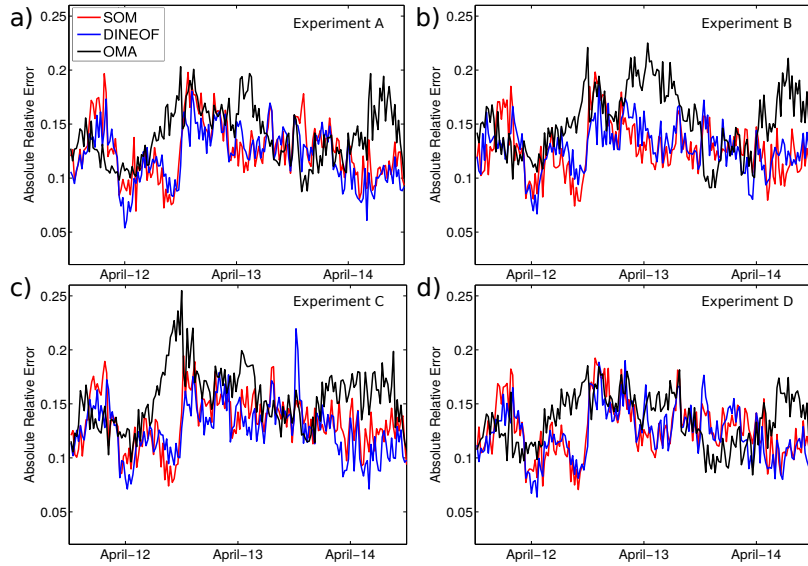
Figure 14. Time series of the spatial average of the pixel by pixel absolute relative error of the RT computed with the reconstructed velocities with respect to the REF-RT.

.

5.4 Residence times

Other Lagrangian quantity suitable to describe transport process is the residence times (RT) (Buffoni et al., 1996; Lipphardt et al., 2006; Hernández-Carrasco et al., 2013). RT is commonly used to characterize the fluid interchange between different oceanic regions and is defined as the interval of time that a particle remains in an area before crossing a particular boundary. In the calculation of RT particles are initially located on the grid points of the HFR velocity field and are integrated in time during 14 days. We consider only 14 days owing to the short period of the available data without missing values (REF field). In these computations we assign the maximum possible value of RT (14 days) to the particles that remain in the area without crossing the pre-selected boundary after the 14 days of integration.

As done for the LCS, a first comparison is performed looking at the spatial distribution of RT obtained from the three different filled HFR datasets. In general, RT maps from the three methodologies are similar to the REF-RT (maps of RT obtained from the reference HFR velocity field). As an example, Figure 13 shows two maps of RT for the experiment A and C corresponding to April, 04, 2013, at 18:00. In this figure we color the initial position of particles in the BoB according to the time they need to escape from the HFR domain. Regions with particles with short residence times are shown in cyan/blue, and initial positions of particles having longer residence times are indicated in light brown. Again these two experiments are representative for the other experiments since the experiments B and D produce RT spatial distribution similar to that shown for experiment A (Figure 13 a). As it can be appreciated, spatial patterns of RT obtained from the filled HF Radar velocity fields are similar to the REF-RT in the experiment A (and also for the experiments B and D, not shown). Only some differences are found in OMA-RT
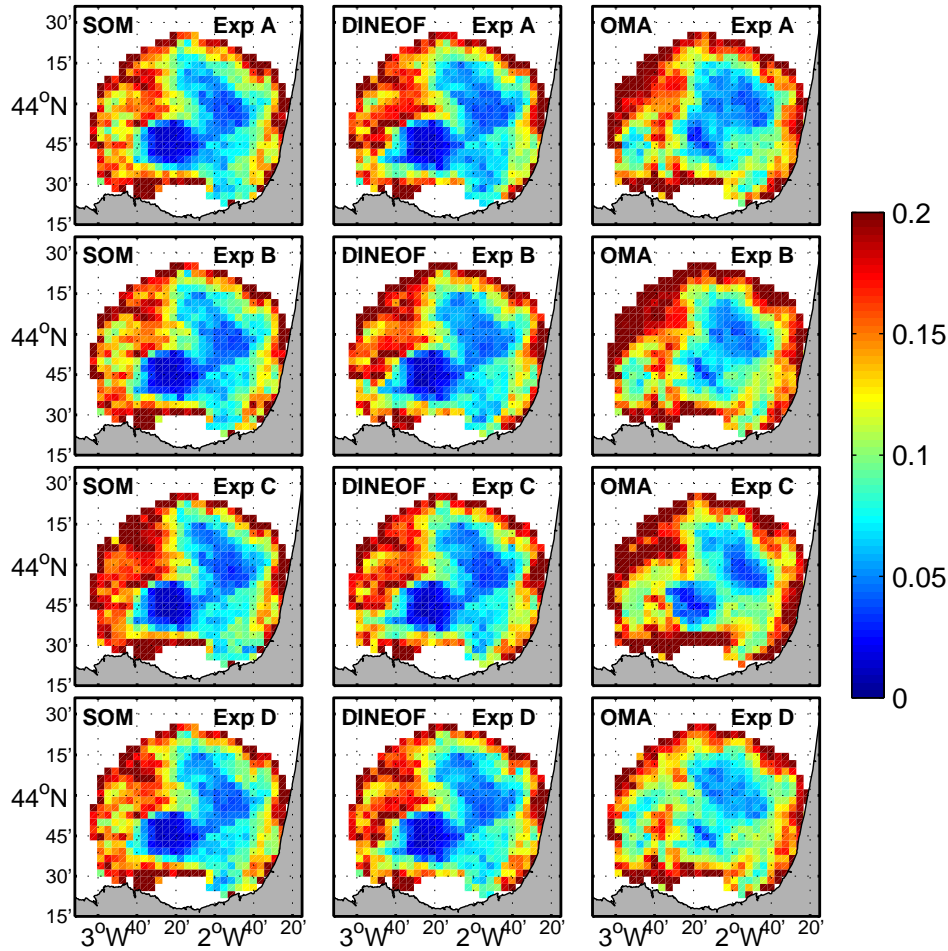
Figure 15. Maps of the time average of the pixel by pixel absolute relative error of the RT computed from the three filled velocities with respect to RT obtained from the reference velocity field.

.

maps compared to REF-RT for the experiment C, as can be seen in Figure 13 b (OMA panel) with higher values of RT in the west and the south-east regions of the HFR domain.

To further analyze the periods when the gap-filling methods introduce more errors in the RT computations we plot in Fig. 14 the time series of the spatial averages of the ARE of the RT. Most of the reconstructed derived RT values approximate REF-RT
5 values, with ARE smaller than 0.2 along the time series. It can be seen that, except at the beginning of April 2012, values of ARE for OMA-RT are larger than SOM-RT and DINEOF-RT, in particular, at the end of April 2012 and at the middle of April 2013 and April 2014. Again, experiment C turns out as the more critical situation of gap distribution to be reconstructed, reaching the largest values of ARE (around 0.25).

Table 4. Mean absolute relative error (ARE) and Mean bias (MB) of the RT obtained using reconstructed HFR velocities from the three methodologies with respect to the REF-RT for all the experiments. A total of 156240 RT values are used in the computations.

		SOM	DINEOF	OMA
Experiment A	ARE	0.12	0.12	0.14
	MB (hours)	5.3	5.4	8.1
Experiment B	ARE	0.13	0.13	0.15
	MB (hours)	5.0	4.3	6.4
Experiment C	ARE	0.13	0.13	0.16
	MB (hours)	7.8	4.8	7.8
Experiment D	ARE	0.13	0.12	0.14
	MB (hours)	5.9	4.5	0.7

In order to reveal regions where the effect of the reconstruction on the RT is higher we compute the time averaged relative error for all experiments (Figure 15). This figure shows that, as for the LCS comparison, regions of accumulated errors are the same for SOM and DINEOF and that this spatial distribution is quite similar for the four experiments. OMA shows different regions with large errors, being the method with the greatest number of pixels with large error. A common feature is that the three methods yield large errors near the southern coastline and in the west and northwest area of the HFR domain. It suggests that the three methods remove some dynamical features in this region. For points located in central regions (around 2°W and 44°N) values of RT derived from the reconstructed velocities approximate better the REF-RT values. The greater availability of data over this region could explain this agreement in the RT computations.

To finish this section, we summarize in Table 4 the results of the ARE and ME of RT averaged over all the RT values. Although ARE is slightly greater in the case of the OMA than using SOM and DINEOF, in general, these errors are low in all cases, being 0.16 the maximum ARE obtained over all the experiments. The absolute error, is smaller for SOM and DINEOF (between 0.12 and 0.13 for both cases) and slightly larger for OMA (between 0.13-0.16). Furthermore the ARE for SOM-RT and DINEOF-RT are quite identical. In all cases the MB are positive, meaning that RT are overestimated. Largest values of MB are found, in average, for OMA-RT (MB ranging from 0.7 hours for experiment D to 8.1 hours for experiment A), followed by SOM-RT (MB ranging from 5.0 hours for experiment B to 7.8 hours for experiment C) and finally by DINEOF-RT (MB ranging from 4.3 hours for experiment B to 5.4 hours for experiment A).

6 Discussion and conclusions

We have investigated the performance of HFR gap-filling methodologies by studying the reliability of some basic Lagrangian metrics for the assessment of the coastal dynamical properties when they are computed using reconstructed velocity fields. A sensitivity test has been carried out through four experiments including the most common scenarios of data gaps observed in HFR systems, i.e., hardware failures, communication interruptions, particular environmental conditions affecting the detection of the signal, sea state, etc.

In contrast to other comparative studies of different gap-filling methodologies based on Eulerian differences (Yaremchuk and Sentchev, 2009; Fredj et al., 2016), we have focused on the propagation of the errors introduced in the reconstruction of the velocity fields through the Lagrangian metrics. We found that the relative errors (up to 43%, 38% and 57% in the case of SOM, DINEOF and OMA methods, respectively, in the worst gap-scenario corresponding to one antenna failure) are reduced in the Lagrangian diagnosis. The largest errors for the LCS computations are up to 22%, 22% and 27% and for the RT up to 13%, 13% and 16% obtained with SOM, DINEOF and OMA reconstructed velocities, respectively.

The four experiments based on different grouping of missing values demonstrate that even for spatially severe and persistent gaps, the Lagrangian diagnoses obtained from FSLE fields and RT are robust representations of the surface dynamics in coastal basins. Our results show that even when a large number of pixels is missing the FSLEs computations still give an accurate picture of the oceanic transport properties. The velocity fields filled by the three methods analyzed do not introduce artifacts in the Lagrangian computations. The robustness of the Lagrangian diagnoses against errors in the velocity data could explain the low relative error in the FSLE and LCS computations from the reconstructed velocities (Hernández-Carrasco et al., 2011).

While DINEOF presents the lowest errors in the Eulerian frame, SOM is the method with lowest errors in the trajectories, LCS and RT computations. DINEOF and SOM reconstruction methods are based on patterns of the velocity field extracted from statistical concepts. These methods strongly depend on the number of modes/neurons used in the reconstruction. The greater the number of modes/neurons, the less smoothed the pattern will be. However even when using a large size of the neural network or number of modes, these methods are prone to filter the velocity field removing some small scale dynamical features, and in some cases the resulting patterns are a smoothed representation of the real dynamics. DINEOF and SOM also depend on the choice of the modes or patterns. This could explain the large number of points out of the main cloud in the scatter plot shown in Figure 5 for DINEOF in experiment C. These outliers can propagate the error in the computations of trajectories, explaining the difference between the Eulerian and Lagrangian comparison of the DINEOF and SOM methods. In the SOM methodology the fact that each neuron is composed of velocity fields at three different times could increase the probability of using a more suitable pattern for the reconstruction, in particular, in the cases where there is a large number of missing points (i.e. experiment C, failure of antenna).

On the other hand, OMA is a geometrical approach that uses a combination of irrotational and incompressible field configurations and the spatial shape of the HFR domain to decomposed the HFR velocity field. This technique also depends on the choice of the modes and the number of modes. In general, since only a finite number of modes is computed, an arbitrariness is introduced in the selection of the modes, that is, the real velocity is projected into a subspace of modes that are either tangent

to the coastline or to the open boundary. Using a small number of modes could affect the results of the reconstruction obtaining a velocity field far away from the HFR data but with very simple features. In situations where the flow patterns are simple and quasi-permanent, the use of a few modes is able to capture these main features. In contrast, if a large number of modes is used, the reconstructed field matches the HFR data, but the data are not sufficiently filtered and smoothed, introducing some

5 dynamical features or even artifacts, which may not exist in the real flow. In our case, the coastline in the area of the HFR coverage is relatively large originating an increase in the number of modes tangent to the coast to the detriment of the OMA open boundary modes, therefore, conditioning the resulting inferred velocity field. As explained in section 3, the constraints applied in the OMA can limit the representation of localized small-scale features as well as flow structures near open boundaries. Besides, as discussed in Kaplan and Lekien (2007), difficulties may arise when the spatial gap size is larger than the

10 smallest resolved length scale, explaining why the weaker results are obtained when only data from one antenna is available. The study of the effect of individual sources of errors on the reconstruction is not trivial and depends on the coherence and persistence of the dynamical features as well as on the full knowledge of the dynamical scales involved in the tracers motion. Further analyses are needed to answer these questions, but this is out of scope of this paper and should be addressed in future studies.

15 In general, regions less affected by missing points are located in the middle of the HFR domain. The large coverage of data can explain this spatial distribution. Moreover, large errors are concentrated in the west part of the HFR domain, likely induced by the high variability of the flow in this region, increasing the effect of the velocity error on the trajectories. The low number of gaps in the central part of the HFR domain in the experiment B and the separation of the missing points randomly distributed in the experiment D can explain the similarity in the Lagrangian diagnosis obtained in these experiments for the

20 three gap-filling methodologies. Experiment C, simulating the failure of one of the two antenna is the worst-case gap scenario, obtaining the largest errors in all the Lagrangian computations according to the errors found in the Eulerian comparisons.

The time period selected (April) represents the dynamical conditions during spring time. This is a transition period between the winter (where the persistent Iberian Poleward Current dominates) and summer where low energy and stable conditions are observed (Solabarrieta et al., 2014). Applying the methodologies over this period, characterized by high dynamical variability,

25 allows to avoid specific circulation patterns ensuring the application of the results to other areas. However analysis in different regions and periods is required to corroborate this statement.

Concerning the temporal distribution of gaps, we have introduced gaps in the 50% of the time period which is much higher than the 10-20% of the time failures accepted in a well-functioning system. Nevertheless, this study is more focused on the spatial gaps and further analysis should be done to analyze the limit of applicability of each method regarding the temporal

30 horizon.

All the results reported in this study can not be extended to HFR systems working at different frequencies and resolutions. HFR working at different frequencies captures dynamical features at different scales that could be altered during the reconstruction process. Further studies using data from different HFR systems and regions characterized with different dynamical conditions should be performed to address this question. For instance as said above some SOM and DINEOF modes used

35 in the reconstruction are smoothed representations of the real dynamics and they could remove some small scale dynamical

processes. However, these results are illustrative of the high performance of the gap-filling methodologies in providing reliable HFR velocities for a Lagrangian assessment of the ocean coastal dynamics.

Contrary to SOM and, to a lesser extent, to DINEOF, one of the main advantages of using OMA is that this method does not need long time series of data and therefore it can be used immediately after installing the HFR system. Also, OMA allows the reconstruction of total velocities in areas of large GDOP error, which also represents an advantage since it enables a larger spatial coverage. Besides DINEOF has the advantage of not requiring long training datasets and of not having subjective parameters. On the other hand, SOM is able to introduce nonlinear correlations in the computation of the patterns.

These experiments also show that the developed SOM methodology is suitable to encode properly the dynamical patterns present in turbulent flows. This is a very promising result and opens up new possibilities for applying this methodology for the inference of HFR currents the periods when data is not available. Although the performance of SOM and DINEOF methods is high, it is worthy to note that in this study we have used a simple algorithm based only on the HFR dataset, which will be improved in future works performing the analysis on HFR velocities coupled with other oceanic variables. Moreover, a more rigorous sensitive analysis is needed to know the temporal coverage needed to obtain reliable reconstructed velocity fields and to optimize the algorithm in terms of errors and computational cost.

A good approximation to obtain an optimal reconstruction of the velocity field could be the combination of these methodologies. For instance, first filling the gaps of the radial velocities through SOM or DINEOF and then reconstructing the total velocities using OMA would allow to obtain a wider coverage without removing small scale features.

Author contributions. I.H-C. conceived the idea of the study with the support of A.O, A.R and L.S; I.H-C developed the SOM methodology with the support of A.O; I.H-C produced the SOM HFR velocities and conduced all the Lagrangian calculations and comparisons; A.O performed the Eulerian comparison; L.S and A.R developed the method for grouping the gap scenarios, introduced the gaps in the HFR data and provided the OMA HFR velocities; G.E provided the DINEOF HFR velocities; I.H-C wrote the ms with contributions made by L.S, A.O, A.R and G.E.

Competing interests. Authors declare that there are no competing interests.

Acknowledgements. This study has been supported by the JERICO-NEXT project, funded by the European Union's Horizon 2020 research and innovation programme under grant agreement No 654410. I. Hernandez-Carrasco acknowledges the Juan de la Cierva contract funded by the Spanish Government. The work of A. Rubio was partially supported by the LIFE-LEMA project (LIFE15 ENV/ES/000252), the Directorate of Emergency Attention and Meteorology of the Basque Government and the Department of Environment, Regional Planning, Agriculture and Fisheries of the Basque Government (Marco Program).

References

Alvera-Azcárate, A., Barth, A., Rixen, M., and Beckers, J. M.: Reconstruction of incomplete oceanographic data sets using empirical orthogonal functions: application to the Adriatic Sea surface temperature, Ocean Modelling, 9, 325–346, https://doi.org/10.1016/j.ocemod.2004.08.001, 2005.

5   Alvera-Azcárate, A., Barth, A., Beckers, J. M., and Weisberg, R. H.: Multivariate reconstruction of missing data in sea surface temperature, chlorophyll, and wind satellite fields, Journal of Geophysical Research-Oceans, 112, https://doi.org/10.1029/2006JC003660, 2007.

Alvera-Azcárate, A., Barth, A., Sirjacobs, D., and Beckers, J. M.: Enhancing temporal correlations in EOF expansions for the reconstruction of missing data using DINEOF, Ocean Science, pp. 475–485, https://doi.org/10.5194/os-5-475-2009, 2009.

Alvera-Azcárate, A., Vanhellemont, Q., Ruddick, K., Barth, A., and Beckers, J.-M.: Analysis of high frequency geostationary ocean colour data using DINEOF, Estuarine, Coastal and Shelf Science, 159, 28 – 36, https://doi.org/10.1016/j.ecss.2015.03.026, 2015.

10   Alvera-Azcárate, A., Barth, A., Parard, G., and Beckers, J.-M.: Analysis of SMOS sea surface salinity data using DINEOF, Remote Sensing of Environment, 180, 137 – 145, https://doi.org/10.1016/j.rse.2016.02.044, 2016.

Aurell, E., Boffetta, G., Crisanti, A., Paladin, G., and Vulpiani, A.: Predictability in the large: an extension of the Lyapunov exponent, J. Phys. A, 30, 1–26, https://doi.org/10.1088/0305-4470/30/1/003, 1997.

15   Barrick, D. E.: Geometrical Dilution of Statistical Accuracy (GDOSA) in Multi-Static HF Radar Networks, Codar Ocean Sensors., http://www.codaros.com/Manuals/SeaSonde/Docs/Informative/, 2002.

Barrick, D. E., Evans, M. W., and Weber, B. L.: Ocean Surface current mapped by radar, Science, 198, 138–144, 1977.

Basterretxea, G., Font-Muñoz, J. S., Salgado-Hernanz, P. M., Arrieta, J., and Hernández-Carrasco, I.: Patterns of chlorophyll interannual variability in Mediterranean biogeographical regions, Remote Sensing of Environment, 215, 7 – 17, https://doi.org/10.1016/j.rse.2018.05.027,

20   2018.

Bauer, J. E., Cai, W.-J., Raymond, P. A., Bianchi, T. S., Hopkinson, C. S., and Regnier, P. A. G.: The changing carbon cycle of the coastal ocean, Nature, 514, 61–70, https://doi.org/10.1038/nature12857, 2013.

Beckers, J. M. and Rixen, M.: EOF calculations and data filling from incomplete oceanographic datasets, Journal of Atmospheric and Oceanic Technology, 20, 1839–1856, https://doi.org/10.1175/1520-0426(2003)020, 2003.

25   Beckers, J.-M., Barth, A., Tomazic, I., and Alvera-Azcárate, A.: A method to generate fully multi-scale optimal interpolation by combining efficient single process analyses, illustrated by a DINEOF analysis spiced with a local optimal interpolation, Ocean Science, 10, 845–862, https://doi.org/10.5194/os-10-845-2014, 2014.

Bellomo, L., Griffa, A., Cosoli, S., Falco, P., Gerin, R., Iermano, I., Kalampokis, A., Kokkini, Z., Lana, A., Magaldi, M., Mamoutos, I., Mantovani, C., Marmain, J., Potiris, E., Sayol, J., Barbin, Y., Berta, M., Borghini, M., Bussani, A., Corgnati, L., Dagneaux, Q., Gaggelli, J., Guter-

30   man, P., Mallarino, D., Mazzoldi, A., Molcard, A., Orfila, A., Poulain, P.-M., Quentin, C., Tintoré, J., Uttieri, M., Vetrano, A., Zambianchi, E., and Zervakis, V.: Toward an integrated HF radar network in the Mediterranean Sea to improve search and rescue and oil spill response: the TOSCA project experience, Journal of Operational Oceanography, 8, 95–107, https://doi.org/10.1080/1755876X.2015.1087184, 2015.

Bettencourt, J., López, C., Hernández-García, E., Montes, I., Sudre, J., Dewitte, B., Paulmier, A., and Garçon, V.: Boundaries of the Peruvian oxygen minimum zone shaped by coherent mesoscale dynamics, Nature Geoscience, 8, 937–940, https://doi.org/doi:10.1038/ngeo2570,

35   2015.

Bjorkstedt, E. and Roughgarden, J.: Larval Transport and Coastal Upwelling: An Application of HF Radar in Ecological Research, Oceanography, 10, 64–67, 1997.

Boffetta, G., Celani, A., Cencini, M., Lacorata, G., and Vulpiani, A.: Non-asymptotic properties of transport and mixing, Chaos, 10, 50–60, https://doi.org/10.1063/1.166475, 2000.

Buffoni, G., Cappelletti, A., and Cupini, E.: Advection-diffusion processes and residence times in semi-enclosed marine basins, Int. J. Numer. Methods Fluids, 22, 1–23, 1996.

5 Callies, J. and Ferrari, R.: Interpreting Energy and Tracer Spectra of Upper-Ocean Turbulence in the Submesoscale Range (1–200 km), Journal of Physical Oceanography, 43, 2456–2474, https://doi.org/10.1175/JPO-D-13-063.1, 2013.

Capet, X., McWilliams, J. C., Molemaker, M. J., and Shchepetkin, A. F.: Mesoscale to Submesoscale Transition in the California Current System. Part I: Flow Structure, Eddy Flux, and Observational Tests, Journal of Physical Oceanography, 38, 29–43, https://doi.org/10.1175/2007JPO3671.1, 2008.

10 Cavazos, T., Comrie, A. C., and Liverman, D. M.: Intraseasonal variability associated with wet monsoons in southeast Arizona, J. Clim., 15, 2477–2490, 2002.

Chapman, R. D., Shay, L. K., Graber, H. C., Edson, J. B., Karachintsev, A., Trump, C. L., and Ross, D. B.: On the accuracy of HF radar surface current measurements: Intercomparisons with ship-based sensors, Journal of Geophysical Research: Oceans, 102, 18 737–18 748, https://doi.org/10.1029/97JC00049.

15 Charantonis, A., F., B., and Thiria, S.: Retrieving the evolution of vertical profiles of chlorophyll-a from satellite observations, by using hidden Markov models and self-organizing maps, Remote Sens. Environ, 163, 229–239, 2015.

Choi, J., Bracco, A., Barkan, R., Shchepetkin, A., McWilliams, J., and Molemaker, J.: Submesoscale Dynamics in the Northern Gulf of Mexico. Part III: Lagrangian Implications, Journal of Physical Oceanography, 47, 2361–2376, https://doi.org/10.1175/JPO-D-17-0036.1, 2017.

20 Chon, T.-S.: Self-Organizing Maps applied to ecological sciences, Ecological Informatics, 6, 50 – 61, https://doi.org/10.1016/j.ecoinf.2010.11.002, special Issue: 5th Anniversary, 2011.

Cianelli, D., D'Alelio, D., Uttieri, M., Sarno, D., Zingone, A., Zambianchi, E., and d'Alcalá, M. R.: Disentangling physical and biological drivers of phytoplankton dynamics in a coastal system, Scientific Reports, 7, 15 868, https://doi.org/10.1038/s41598-017-15880-x, 2017.

Cloern, J. E., Foster, S. Q., and Kleckner, A. E.: Phytoplankton primary production in the world's estuarine-coastal ecosystems, Biogeosciences, 11, 2477–2501, https://doi.org/10.5194/bg-11-2477-2014, 2014.

Corrado, R., Lacorata, G., Paratella, L., Santoleri, R., and Zambianchi, E.: General characteristics of relative dispersion in the ocean, Sci. Rep., 7, 46 291, https://doi.org/10.1038/srep46291, 2017.

Esnaola, G., Sáenz, J., Zorita, E., Lazure, P., Ganzedo, U., Fontán, A., Ibarra-Berastegi, G., and Ezcurra, A.: Coupled air-sea interaction patterns and surface heat-flux feedback in the Bay of Biscay, Journal of Geophysical Research-Oceans, 117, https://doi.org/10.1029/2011JC007692, 2012.

30 Fredj, E., Roarty, H., Kohut, J., Smith, M., and Glenn, S.: Gap Filling of the Coastal Ocean Surface Currents from HFR Data: Application to the Mid-Atlantic Bight HFR Network, Journal of Atmospheric and Oceanic Technology, 33, 1097–1111, https://doi.org/10.1175/JTECH-D-15-0056.1, 2016.

Ganzedo, U., Alvera-Azcárate, A., Esnaola, G., Ezcurra, A., and Sáenz, J.: Reconstruction of sea surface temperature by means of 35 DINEOF: a case study during the fishing season in the Bay of Biscay, International Journal of Remote Sensing, 32, 933 – 950, https://doi.org/10.1080/01431160903491420, 2011.

Griffa, A., Haza, A., Özgökmen, T., Molcard, A., Taillandier, V., Schroeder, K., Chang, Y., and Poulain, P.-M.: Investigating transport pathways in the ocean, Deep Sea Research Part II: Topical Studies in Oceanography, 85, 81 – 95, https://doi.org/10.1016/j.dsr2.2012.07.031, 2013.

Guanche, Y., Mínguez, R., and Méndez, F. J.: Autoregressive logistic regression applied to atmospheric circulation patterns, Climate Dynamics, 42, 537–552, https://doi.org/10.1007/s00382-013-1690-3, 2014.

Haidvogel, D., Blanton, J., Kindle, J., and Lynch, D.: Coastal Ocean Modeling: Processes and Real-Time Systems, Oceanography, 13(1), 35–46, 2000.

Hales, B., Strutton, P. G., Saraceno, M., Letelier, R., Takahashi, T., Feely, R. A., Sabine, C. L., and Chavez, F.: Satellite-based prediction of pCO_2 in coastal waters of the eastern North Pacific, Prog. Oceanogr., 103, 1–15, 2012.

Haller, G.: Lagrangian Coherent Structures, Annual Review of Fluid Mechanics, 47, 137 – 162, https://doi.org/10.1146/annurev-fluid-010313-141322, 2015.

Hastie, T., Tibshirani, R., and Friedman, J.: The Elements of Statistical Learning: Data Mining, Inference, and Prediction., Springer, second edition, 2009.

Haza, A. C., Poje, A. C., Özgökmen, T. M., and Martin, P.: Relative dispersion from a high-resolution coastal model of the Adriatic Sea, Ocean Modell., 22, 48–65, https://doi.org/10.1016/j.ocemod.2008.01.006, 2008.

Haza, A. C., Özgökmen, T. M., Griffa, A., Molcard, A., Poulain, P.-M., and Peggion, G.: Transport properties in small-scale coastal flows: relative dispersion from VHF radar measurements in the Gulf of La Spezia, Ocean Dynamics, 60, 861–882, https://doi.org/10.10007/s10236-010-0301-7, 2010.

Hernández-Carrasco, I. and Orfila, A.: The role of an intense front on the connectivity of the western Mediterranean sea: the Cartagena-Tenes front, Journal of Geophysical Research: Oceans, https://doi.org/10.1029/2017JC013613, 2018b.

Hernández-Carrasco, I., López, C., Hernández-García, E., and Turiel, A.: How reliable are finite-size Lyapunov exponents for the assessment of ocean dynamics?, Ocean Modelling, 36, 208 – 218, https://doi.org/10.1016/j.ocemod.2010.12.006, 2011.

Hernández-Carrasco, I., López, C., Hernández-García, E., and Turiel, A.: Seasonal and regional characterization of horizontal stirring in the global ocean, Journal of Geophysical Research: Oceans, 117, C10 007, https://doi.org/doi:10.1029/2012JC008222, 2012.

Hernández-Carrasco, I., López, C., Orfila, A., and Hernández-García, E.: Lagrangian transport in a microtidal coastal area: the Bay of Palma, island of Mallorca, Spain, Nonlinear Processes in Geophysics, 20, 921–933, https://doi.org/10.5194/npg-20-921-2013, 2013.

Hernández-Carrasco, I., Rossi, V., Hernández-García, E., Garçon, V., and López, C.: The reduction of plankton biomass induced by mesoscale stirring: A modeling study in the Benguela upwelling, Deep Sea Research Part I: Oceanographic Research Papers, 83, 65 – 80, https://doi.org/10.1016/j.dsr.2013.09.003, 2014.

Hernández-Carrasco, I., Orfila, A., Rossi, V., and Garçon, V.: Effect of small-scale transport processes on phytoplankton distribution in coastal seas, Scientific Reports, 8:8613, https://doi.org/10.1038/s41598-018-26857-9, 2018.

Joseph, B. and Legras, B.: Relation between Kinematic Boundaries, Stirring, and Barriers for the Antarctic Polar Vortex, J. Atm. Sci., 59, 1198–1212, https://doi.org/10.1175/1520-0469(2002)059<1198:RBKBSA>2.0.CO;2, 2002.

Kalampokis, A., Uttieri, M., Poulain, P. M., and Zambianchi, E.: Validation of HF Radar-Derived Currents in the Gulf of Naples With Lagrangian Data, IEEE Geoscience and Remote Sensing Letters, 13, 1452–1456, https://doi.org/10.1109/LGRS.2016.2591258, 2016.

Kaplan, D. M. and Lekien, F.: Spatial interpolation and filtering of surface current data based on open-boundary modal analysis, Journal of Geophysical Research: Oceans, 112, https://doi.org/10.1029/2006JC003984, c12007, 2007.

Klein, P., Hua, B., , Lapeyre, G., Capet, X., Gentil, S. L., and Sasaki, H.: Upper ocean turbulence from a high 3-D resolution simulations, Journal of Physical Oceanography, 38, 1748–1763, 2008.

Kohonen, T.: Self-Organized Formation of Topologically Correct Feature Maps, Biological Cybernetics, 43, 59–69, 1982.

Kohonen, T.: Self-Organizing Maps, Springer 2nd edn, Heidelberg, Germany, 1997.

5   Lacorata, G., Aurell, E., and Vulpiani, A.: Drifter dispersion in the Adriatic Sea: Lagrangian data and chaotic model, Ann. Geophysicae, 19, 121–129, https://doi.org/10.5194/angeo-19-121-2001, 2001.

Lana, A., Marmain, J., Fernández, V., Tintoré, J., and Orfila, A.: Wind influence on surface current variability in the Ibiza Channel from HF Radar, Ocean Dynamics, 66, 483–497, https://doi.org/10.1007/s10236-016-0929-z, http://dx.doi.org/10.1007/s10236-016-0929-z, 2016.

Lekien, F., Coulliette, C., Mariano, A. J., Ryan, E. H., Shay, L. K., Haller, G., and Marsden, J.: Pollution release tied to invariant manifolds:
10   A Case study for the coast of Florida, Physica D., 210, 1–20, https://doi.org/10.1016/j.physd.2005.06.023, 2005.

Lipphardt, B., Jr., Small, D., Kirwan, A., Jr., Wiggins, S., Ide, K., Grosch, C., and Paduan, J.: Synoptic Lagrangian maps: Application to surface transport in Monterey Bay, Journal of Marine Research, 64, 221–247, 2006.

Liu, Y. and Weisberg, R. H.: Patterns of ocean current variability on the West Florida Shelf using the self-organizing map, Journal of Geophysical Research: Oceans, 110, https://doi.org/10.1029/2004JC002786, c06003, 2005.

15   Liu, Y., Weisberg, R. H., and Mooers, C. N. K.: Performance evaluation of the self-organizing map for feature extraction, Journal of Geophysical Research: Oceans, 111, https://doi.org/10.1029/2005JC003117, c05018, 2006.

Liu, Y., Weisberg, R. H., Vignudelli, S., and Mitchum, G. T.: Patterns of the loop current system and regions of sea surface height variability in the eastern Gulf of Mexico revealed by the self-organizing maps, Journal of Geophysical Research: Oceans, 121, 2347–2366, https://doi.org/10.1002/2015JC011493, 2016.

20   Lumpkin, R. and Elipot, S.: Surface drifter pair spreading in the North Atlantic, Journal of Geophysical Research: Oceans, 115, https://doi.org/10.1029/2010JC006338, c12017, 2010.

Molcard, A., Poulain, P., Forget, P., Griffa, A., Barbin, Y., Gaggelli, J., Maistre, J. D., and Rixen, M.: Comparison between VHF radar observations and data from drifter clusters in the Gulf of La Spezia (Mediterranean Sea), Journal of Marine Systems, 78, S79 – S89, https://doi.org/https://doi.org/10.1016/j.jmarsys.2009.01.012, 2009.

25   Nikkilä, J., Törönen, P., Kaski, S., Castrén, J. V. E., and Wong, G.: Analysis and visualization of gene expression data using self-organizing maps, Neural Netw., 15(8-9), 953–966, 2002.

Paduan, J. D. and Washburn, L.: High-frequency radar observations of ocean surface currents, Ann. Rev. Mar. Sci., 5, 115–136, https://doi.org/10.1146/annurev-marine-121211-172315, 2013.

Pauly, D., Alder, J., Booth, S., Cheung, W., Christensen, V., Close, C., Sumaila, U., Swartz, W., Tavakolie, A., Watson, R., Wood, L.,
30   and Zeller, D.: Fisheries in Large Marine Ecosystems: Descriptions and Diagnoses, in: The UNEP Large Marine Ecosystem Report: a Perspective on Changing Conditions in LMEs of the World's Regional Seas. UNEP Regional Seas Reports and Studies No. 182, edited by Uijttewaal, W. and Jirka, G., pp. 23–40, K. Sherman and G. Hempel (eds.), 2008.

Poje, A. C., Özgökmen, T. M., Lipphardt, B. L., Haus, B. K., Ryan, E. H., Haza, A. C., Jacobs, G. A., Reniers, A. J. H. M., Olascoaga, M. J., Novelli, G., Griffa, A., Beron-Vera, F. J., Chen, S. S., Coelho, E., Hogan, P. J., Kirwan, A. D., Huntley, H. S., and Mariano,
35   A. J.: Submesoscale dispersion in the vicinity of the Deepwater Horizon spill, Proceedings of the National Academy of Sciences, 111, 12 693–12 698, https://doi.org/10.1073/pnas.1402452111, 2014.

QARTOD: Manual for Real-Time Quality Control of In-Situ Surface Wave Data: a Guide to Quality Control and Quality Assurance of In-Situ Surface Wave Observations Version 2.0., U.S. Department of Commerce, National Oceanic and Atmospheric Administration, National Ocean Service, Integrated Ocean Observing System Silver Spring, MD, 2015.

Richardson, A. J., Risien, C., and Shillington, F. A.: Using self-organizing maps to identify patterns in satellite imagery, Prog. Oceanogr., 59, 223–239, 2003.

Rubio, A., Reverdin, G., Fontán, A., González, M., and Mader, J.: Mapping near-inertial variability in the SE Bay of Biscay from HF radar data and two offshore moored buoys, Geophysical Research Letters, 38, L19 607, https://doi.org/10.1029/2011GL048783, 2011.

Rubio, A., Mader, J., Corgnati, L., Mantovani, C., Griffa, A., Novellino, A., Quentin, C., Wyatt, L., Schulz-Stellenfleth, J., Horstmann, J., Lorente, P., Zambianchi, E., Hartnett, M., Fernandes, C., Zervakis, V., Gorringe, P., Melet, A., and Puillat, I.: HF Radar Activity in European Coastal Seas: Next Steps toward a Pan-European HF Radar Network, Frontiers in Marine Science, 4, 8, https://doi.org/10.3389/fmars.2017.00008, 2017.

Rubio, A., Caballero, A., Orfila, A., Hernández-Carrasco, I., Ferrer, L., González, M., Solabarrieta, L., and Mader, J.: Eddy-induced cross-shelf export of high Chl-a coastal waters in the SE Bay of Biscay, Remote Sensing of Environment, 205, 290 – 304, https://doi.org/https://doi.org/10.1016/j.rse.2017.10.037, 2018.

Schmidt, R. O.: Multiple emitter location and signal parameter estimation, IEEE Transactions Antennas Propagation, 34, 276–280, 1986.

Schroeder, K., Haza, A., Griffa, A., Özgökmen, T., Poulain, P., Gerin, R., Peggion, G., and Rixen, M.: Relative dispersion in the Liguro-Provençal basin: From sub-mesoscale to mesoscale, Deep Sea Research Part I: Oceanographic Research Papers, 58, 209 – 228, https://doi.org/http://dx.doi.org/10.1016/j.dsr.2010.11.004, http://www.sciencedirect.com/science/article/pii/S0967063710002323, 2011.

Shadden, S. C., Lekien, F., Paduan, J., Chavez, F., and Marsden, J. E.: The correlation between surface drifters and coherent structures based on high-frequency radar data in Monterey Bay, Deep Sea Res II. Top Stud Oceanogr, 56, 161–172, 2009.

Solabarrieta, L., Rubio, A., Castanedo, S., Medina, R., Fontán, A., González, M., Fernández, V., Charria, G., and Hernández, C.: Surface water circulation patterns in the southeastern Bay of Biscay: New evidences from HF radar data, Continental Shelf Research, 74, 60–76, 2014.

Solabarrieta, L., Rubio, A., Cárdenas, M., Castanedo, S., Esnaola, G., Méndez, F. J., Medina, R., and Ferrer, L.: Probabilistic relationships between wind and surface water circulation patterns in the SE Bay of Biscay, Ocean Dynamics, 65, 1289–1303, https://doi.org/10.1007/s10236-015-0871-5, 2015.

Solabarrieta, L., Frolov, S., Cook, M., Paduan, J., Rubio, A., González, M., Mader, J., and Charria, G.: Skill Assessment of HF Radar-Derived Products for Lagrangian Simulations in the Bay of Biscay, Journal of Atmospheric and Oceanic Technology, 33, 2585–2597, https://doi.org/10.1175/JTECH-D-16-0045.1, 2016.

Stewart, R. H. and Joy, J. W.: HF radio measurements of surface currents, Deep Sea Research and Oceanographic Abstracts, 21, 1039 – 1049, https://doi.org/10.1016/0011-7471(74)90066-7, 1974.

Tew Kai, E., Rossi, V., Sudre, J., Weimerskirch, H., López, C., Hernández-García, E., Marsac, F., and Garçon, V.: Top marine predators track Lagrangian coherent structures, Proc. Natl. Acad. Sci. U.S.A., 106, 8245–8250, https://doi.org/10.1073/pnas.0811034106, 2009.

Ullman, D. S., O'Donnell, J., Kohut, J., Fake, T., and Allen, A.: Trajectory prediction using HF radar surface currents: Monte Carlo simulations of prediction uncertainties, Journal of Geophysical Research: Oceans, 111, https://doi.org/10.1029/2006JC003715, 2006.

Vatanen, T., Osmala, M., Raiko, T., Lagus, K., Sysi-Aho, M., Oresic, M., Honkela, T., and Lähdesmäki, H.: Self-organization and missing values in SOM and GTM, Neurocomputing, 147, 60 – 70, https://doi.org/https://doi.org/10.1016/j.neucom.2014.02.061, 2015.

Vesanto, J., Himberg, J., Alhoniemi, E., and Parhankangas, J.: SOM toolbox for Matlab 5, report, Helsinki Univ. of Technol., Finland, 2000.

Volpe, G., Nardelli, B. B., Cipollini, P., Santoleri, R., and Robinson, I. S.: Seasonal to interannual phytoplankton response to physical processes in the Mediterranean Sea from satellite observations, Remote Sensing of Environment, 117, 223 – 235, https://doi.org/10.1016/j.rse.2011.09.020, 2012.

Yaremchuk, M. and Sentchev, A.: Mapping radar-derived sea surface currents with a variational method, Continental Shelf Research, 29, 1711 – 1722, https://doi.org/https://doi.org/10.1016/j.csr.2009.05.016, 2009.